

REGIONAL PUBLIC-HEALTH AND CLIMATE IMPACTS OF COMBUSTION
CARBONACEOUS AEROSOLS

by

SOROUGH ESMAEILI NEYESTANI

(Under the Direction of Rawad Saleh)

ABSTRACT

Combustion sources, including anthropogenic (e.g. vehicles) and natural (e.g. wildland fires) sources are major emitters of carbonaceous aerosol (CA) into the atmosphere. CA, which includes organic aerosol (OA) and black carbon (BC), has a significant effect on the Earth's radiative balance. BC is a strong absorber of solar radiation and exhibits a global warming effect. On the other hand, OA is mixture of organic components with variable optical properties. Some OA components only scatter solar radiation and have a strong cooling effect, while others (brown carbon, BrC) also absorb solar radiation and can have a net cooling or warming effect. This PhD dissertation focuses on improving the understanding of the climate and public health impacts of combustion CAs. The Weather Research and Forecasting model with chemistry (WRF-Chem) is used as a regional climate model. The month of August 2015 featured extensive wildfires in the Northwestern U.S., with the majority of CA, including BrC, over the U.S. dominated by emissions from these wildfires. We performed parallel simulations that (1) did not account for BrC absorption, (2) accounted for BrC absorption, and (3) accounted for BrC absorption as well as its decay due to

photobleaching. A set of optical properties, namely the aerosol absorption optical depth (AAOD) and absorption Ångström exponent (AAE) is used to constrain the model output against observations. We found that accounting for BrC absorption and photobleaching resulted in the best agreement with observations. We also focused on CA emissions from gasoline vehicles. Gasoline direct injection (GDI) engines emit higher levels of BC compared to traditional port fuel injection (PFI) engines. Here, we performed simulations to estimate the aerosol-induced public health and direct radiative effects of shifting the U.S. fleet from PFI to GDI technology. The results show that the total annual deaths in the U.S. attributed to particulate gasoline-vehicle emissions would increase from 855 to 1599 due to shifting from PFI to GDI. Furthermore, the increase in BC associated with the shift would lead to an annual average positive radiative effect over the U.S. of +0.075 W/m², with values as large as +0.45 W/m² over urban regions.

INDEX WORDS: Aerosols, Gasoline Engine, Public-Health, Direct Radiative Effect, Wildland Fire, Brown Carbon, Absorption Ångström Exponent.

REGIONAL PUBLIC-HEALTH AND CLIMATE IMPACTS OF COMBUSTION
CARBONACEOUS AEROSOLS

by

SOROUSH ESMAEILI NEYESTANI

BS, Islamic Azad University - South Tehran, Iran, 2012

MS, The University of Tehran, Iran, 2016,

A Dissertation Submitted to the Graduate Faculty of The University of Georgia in Partial
Fulfillment of the Requirements for the Degree

DOCTOR OF PHILOSOPHY

ATHENS, GEORGIA

2021

© 2021

Soroush Esmaili Neyestani

All Rights Reserved

REGIONAL PUBLIC-HEALTH AND CLIMATE IMPACTS OF COMBUSTION
CARBONACEOUS AEROSOLS

by

SOROUSH ESMAEILI NEYESTANI

Major Professor:	Rawad Saleh
Committee:	John R Schramski
	Sudhagar Mani
	Gabriel J Kooperman

Electronic Version Approved:

Ron Walcott
Vice Provost for Graduate Education and Dean of the Graduate School
The University of Georgia
August 2021

DEDICATION

I dedicate this study to my parents for their unconditional love and support.

ACKNOWLEDGEMENTS

This dissertation would not have been possible without the support and guidance of my advisor Dr. Rawad Saleh. I would like to express my deepest appreciation to him for his patience and encouragement throughout my doctoral research. I am indebted to him because of the time he dedicated to mentor me.

I am very grateful to my dissertation committee members Dr. John R. Schramski, Dr. Sudhagar Mani, and Dr. Gabriel J. Kooperman for their insightful advice and helpful comments.

I also would like to thank my family, friends, and lab members who supported me during my doctoral study.

TABLE OF CONTENTS

	Page
ACKNOWLEDGEMENTS	v
LIST OF TABLES	viii
LIST OF FIGURES	ix
CHAPTER	
1 INTRODUCTION	1
1.1 Background	1
1.2 Emissions from Biomass Burning	2
1.3 Emissions from Gasoline Direct Injection (GDI) Vehicles	4
1.4 Objectives and Chapter Organization	6
2 REVIEW OF THE REPRESENTATION OF BROWN CARBON ABSORPTION IN CLIMATE MODELS	8
3 OBSERVATIONALLY CONSTRAINED REPRESENTATION OF BROWN CARBON EMISSIONS FROM WILDFIRES IN A CHEMICAL TRANSPORT MODEL	12
3.1 Introduction.....	14
3.2 Experimental Design.....	17
3.3 Model Description	19
3.4 Brown Carbon Parameterization.....	21
3.5 Observational Constraints.....	23

3.6 Model-Observation Comparison.....	25
3.7 Conclusions.....	32
4 DIRECT RADIATIVE EFFECT AND PUBLIC HEALTH IMPLICATIONS OF AEROSOL EMISSIONS ASSOCIATED WITH SHIFTING TO GASOLINE DIRECT-INJECTION (GDI) TECHNOLOGIES IN LIGHT-DUTY VEHICLES IN THE UNITED STATES	34
4.1 Introduction.....	35
4.2 Methods.....	38
4.3 Model Results and Discussion	42
5 CONCLUSIONS, FUTURE WORK, AND LIMITATIONS	60
REFERENCES	64
APPENDICES	
A SUPPORTING INFORMATION FOR CHAPTER 3.....	85
B SUPPORTING INFORMATION FOR CHAPTER 4.....	87
B.1 Performance Metrics Calculations	87
B.2 Derivation of Attributable Fraction (AF).....	87
B.3 Calculations Used in Climate-Tradeoff Analysis.....	88
B.4 Figures	90
B.5 Tables	96

LIST OF TABLES

	Page
Table B1: Models and configurations used in WRF-Chem simulations	96
Table B2: Calculated performance metrics (NME, MFE, and RMSE) for monthly- averaged model results.....	97

LIST OF FIGURES

	Page
Figure 3.1: (a) Column burden of carbonaceous aerosol attributed to biomass-burning emissions averaged over the month of August 2015. As evident in the spatial distribution, emissions from Northwestern wildfires constitute the majority of biomass-burning emissions in the simulation period. Black dots show the locations of AERONET stations used in the model-observation comparisons. (b) The fraction of carbonaceous-aerosol column burden attributed to biomass-burning (wildfire) emissions.	18
Figure 3.2: Comparison between monthly average AAOD at 440 nm for August 2015 obtained from AERONET observations and WRF-Chem output with four different model treatments of wildfire carbonaceous aerosol emissions.	26
Figure 3.3: Comparison between monthly average AOD at 440 nm for August 2015 obtained from AERONET observations and WRF-Chem output with four different model treatments of wildfire carbonaceous aerosol emissions.	27
Figure 3.4: Comparison between monthly average AAE for August 2015 obtained from AERONET observations and WRF-Chem output with four different model treatments of wildfire carbonaceous aerosol emissions.	28
Figure 3.5: Comparison between monthly average SSA at 440 nm for August 2015 obtained from AERONET observations and WRF-Chem output with four different model treatments of wildfire carbonaceous aerosol emissions.	29

Figure 3.6: The SSA at 440 nm averaged over the month of August 2015 from WRF-Chem output with four different model treatments of wildfire carbonaceous aerosol emissions. The color dots show the locations and SSA values of AERONET stations used in the model-observation comparisons.31

Figure 3.7: Column burden of SOA averaged over the month of August 2015 from WRF-Chem output with four different model treatments of wildfire carbonaceous aerosol emissions.32

Figure 4.1: Comparison between monthly average BC, OA, and PM_{2.5} surface concentrations ($\mu\text{g}/\text{m}^3$) predicted by the model and obtained from IMPROVE (blue) and CSN (red) observational data for 2011. (a) BC, January. (b) BC, July. (c) OA, January. (d) OA, July. (e) PM_{2.5}, January. (f) PM_{2.5}, July.44

Figure 4.2: Monthly average BC surface concentrations in January (top panels) and July (bottom panels) 2011. Panels (a) and (e), obtained from the “PFI” experiments, correspond to the total BC concentrations. Panels (b) and (f), obtained as the difference between the “PFI” and “no-gasoline” experiments, correspond to the contribution of the 2011 gasoline fleet (PFI) to BC. Panels (c) and (g), obtained as the difference between the “GDI” and “no-gasoline” experiments, correspond to the contribution of gasoline vehicles to BC after shifting to GDI. Panels (d) and (h), obtained as the difference between the “GDI” and “PFI” experiments, correspond to the effect of shifting from PFI to GDI on BC.47

Figure 4.3: Monthly average OA surface concentrations in January (top panels) and July (bottom panels) 2011. Panels (a) and (e), obtained from the “PFI” experiments, correspond to the total OA concentrations. Panels (b) and (f), obtained as the

difference between the “PFI” and “no-gasoline” experiments, correspond to the contribution of the 2011 gasoline fleet (PFI) to OA. Panels (c) and (g), obtained as the difference between the “GDI” and “no-gasoline” experiments, correspond to the contribution of gasoline vehicles to OA after shifting to GDI. Panels (d) and (h), obtained as the difference between the “GDI” and “PFI” experiments, correspond to the effect of shifting from PFI to GDI on OA.48

Figure 4.4: Monthly average $PM_{2.5}$ surface concentrations in January (top panels) and July (bottom panels) 2011. Panels (a) and (e), obtained from the “PFI”

experiments, correspond to the total $PM_{2.5}$ concentrations. Panels (b) and (f), obtained as the difference between the “PFI” and “no-gasoline” experiments, correspond to the contribution of the 2011 gasoline fleet (PFI) to $PM_{2.5}$. Panels (c) and (g), obtained as the difference between the “GDI” and “no-gasoline” experiments, correspond to the contribution of gasoline vehicles to $PM_{2.5}$ after shifting to GDI. Panels (d) and (h), obtained as the difference between the “GDI” and “PFI” experiments, correspond to the effect of shifting from PFI to GDI on $PM_{2.5}$49

Figure 4.5: Annual average attributable fraction (AF) associated with $PM_{2.5}$ emitted by gasoline vehicles. The color scale represents the number of $PM_{2.5}$ -induced deaths per 10,000 all-cause premature deaths. (a) AF associated with baseline gasoline emissions in 2011 (PFI), calculated based on $PM_{2.5}$ concentrations obtained as the difference between the “PFI” and “no-gasoline” experiments. (b) AF associated with gasoline emissions after shifting to GDI, calculated based on $PM_{2.5}$ concentrations obtained as the difference between the “GDI” and “no-gasoline”

experiments. (c) The effect of shifting from PFI to GDI on AF, calculated as the difference between (b) and (a).52

Figure 4.6: Monthly average direct radiative effect (DRE) of carbonaceous aerosols emitted by gasoline vehicles for January (top panels) and July (bottom panels) 2011. The left panels (a and d) correspond to DRE_{PFI} , the DRE associated with the 2011 gasoline fleet (PFI), obtained as the difference in radiative balance between the “PFI” and “no-gasoline” simulations. The middle panels (b and e) correspond to DRE_{GDI} , the DRE associated with the gasoline vehicles after shifting to GDI, obtained as the difference in radiative balance between the “PFI” and “no-gasoline” simulations. The right panels (c and f) correspond to $DRE_{PFI \rightarrow GDI}$, the DRE associated with shifting from PFI to GDI, calculated as the difference between the middle and left panels (equation 4.5).55

Figure A1: (a) OH concentration averaged over the month of August 2015 and averaged over first 8 vertical layers. (b) BrC absorption half-life averaged over the month of August 2015 and averaged over first 8 vertical layers.85

Figure A2: Comparison between monthly average AAOD at 675 nm for August 2015 obtained from AERONET observations and WRF-Chem output with four different model treatments of wildfire carbonaceous aerosol emissions.85

Figure A3: Comparison between monthly average AOD at 675 nm for August 2015 obtained from AERONET observations and WRF-Chem output with four different model treatments of wildfire carbonaceous aerosol emissions.86

Figure A4: Comparison between monthly average SSA at 675 nm for August 2015 obtained from AERONET observations and WRF-Chem output with four different model treatments of wildfire carbonaceous aerosol emissions.86

Figure B1: Comparison of calculated BC (red), OA (green), and PM_{2.5} (purple) MFEs with suggested accuracy levels by Boylan & Russell¹. Circles show calculated MFE based on IMPROVE and triangles show calculated MFE based on CSN network. Filled circles/triangles demonstrate January-averaged, and no-fills are July-averaged.90

Figure B2: Comparison between monthly average surface temperature (K), incoming solar radiation flux (W/m²), and wind speed (m/s) predicted by the model and obtained from CASTNET observational data for 2011. (a) temperature, January. (b) temperature, July. (c) solar radiation, January. (d) solar radiation, July. (e) wind speed, January. (f) wind speed, July.91

Figure B3: The Monthly average isoprene emission (top panels), α -Pinene emission (middle panels), and SOA surface concentrations (bottom panels) in July 2011. Panels (a), (e), and (i), obtained from the “PFI” experiments, correspond to the total biogenic emissions and SOA concentrations. Panels (b), (f), and (j), obtained as the difference between the “PFI” and “no-gasoline” experiments, correspond to the contribution of the 2011 gasoline fleet (PFI) to the biogenic emissions and SOA concentrations. Panels (c), (g), and (k), obtained as the difference between the “GDI” and “no-gasoline” experiments, correspond to the contribution of gasoline vehicles to the biogenic emissions and SOA concentrations after shifting to GDI. Panels (d), (h), and (l), obtained as the difference between the “GDI” and

“PFI” experiments, correspond to the effect of shifting from PFI to GDI on the biogenic emissions and SOA concentrations.	92
Figure B4: The relative difference between January/July and annual average PM _{2.5} concentration, based on a) CSN and b) IMPROVE observations.	93
Figure B5: The relative difference between January/July and annual average carbonaceous (BC + OA) aerosols concentration, based on a) CSN and b) IMPROVE observations.	94
Figure B6: Monthly average surface albedo in a) January and b) July, 2011.	94
Figure B7: Yearly average climate benefits quantified as the radiative effect of the reduction in CO ₂ emissions associated with a global shift from PFI to GDI	95

CHAPTER 1

INTRODUCTION

1.1. Background

Aerosols, also referred to as particulate matter (PM), have significant effects on public health and the climate system. Of special importance is PM with sizes smaller than 2.5 micrometers (PM_{2.5}) due to its ability to penetrate into the lower respiratory tract upon inhalation². Ambient PM_{2.5} is associated with high rates of mortality due to adverse health effects (e.g. cardiopulmonary disease and lung cancer)³. Fann et al.³ estimated 130,000 premature death in the U.S. in 2005 was due to exposure to PM_{2.5}. There is evidence that among PM_{2.5} components, carbonaceous aerosols (CA), emitted from combustion processes including both anthropogenic (e.g. vehicles, industry, domestic heating and cooking) and natural (e.g. wildland fires) sources⁴, are among the most toxic. CA is comprised of black carbon (BC) and organic aerosol (OA), which is also referred to organic carbon (OC) when only accounting for the carbon content of the aerosol. A study by Janssen et al.⁵ suggested that CA, especially BC, is a better indicator for investigating aerosols health risks than PM_{2.5}. They found that 0.55 µg/m³ decrease in BC exposure results in 3.6 months increase in the life expectancy per person while 1.0 µg/m³ decrease in PM_{2.5} exposure results in 21 days increase in the life expectancy⁵. Turner et al.⁶ found that annual anthropogenic BC-induced mortality rate in 2007, ranges from 8,400 to 16,000 in the U.S.⁶.

CA, including OA and BC, has a significant effect on the Earth's radiative balance by scattering and absorbing the solar radiation⁷. BC is a strong absorber of solar radiation with a global warming effect potentially second only to carbon dioxide^{8,9}. On the other hand, some OA components are purely scattering¹⁰ and have a cooling effect, while other components, referred to as brown carbon (BrC), also contribute to absorption of solar radiation¹¹ alongside BC.

1.2. Emissions from Biomass Burning

Emissions from wildland fires are associated with significant impacts on public health¹²⁻¹⁴ and the climate^{15,16}. On the other hand, wildland fires they play an essential ecological role that benefits natural resources and promotes ecosystem health and resilience^{17,18}. This tradeoff renders planning for the management and mitigation of wildland fires a major challenge¹⁸, especially due to the chaotic nature of open fires which makes model predictions of their public-health and climate impacts highly uncertain^{12,15,19}. Wildland fires encompass wildfires, which are usually ignited unintentionally, and prescribed fires¹⁸. On average in the U.S., prescribed fires (mostly in the Southeastern U.S.) and wildfires (mostly in the Western U.S.) cover similar burned areas annually of ~3 million ha each, though Western wildfires exhibit significant year-to-year variability¹² and have been increasing in intensity due to increase in global temperatures and drought episodes²⁰. With the continued decrease in anthropogenic emissions driven by emission standards and regulation²¹, the fraction of air pollutants attributed to wildland fires has been steadily increasing and is projected to continue to do so in the future²².

Wildland fires are major emitters of CA, including OA and BC. Numerous laboratory studies^{23–25} and field measurements^{26–28} have shown that OA from wildland fires is light-absorbing, and is categorized as BrC^{29–31}. BrC is comprised of various species with a wide range of light-absorption properties, usually quantified using the imaginary part of the refractive index (k). On average, BrC emitted from biomass burning (including wildland fires) exhibits mid-visible k values that are one to two orders of magnitude smaller than k of BC³¹. However, BrC emissions are usually one to two orders of magnitude larger than BC³², thus atmospheric BrC absorption is potentially equally important to BC. Furthermore, BrC exhibits absorption spectra that are largely skewed toward shorter visible and UV wavelengths, which can have important implications for photochemistry^{33,34}.

Representing BrC absorption in chemical transport models is challenging. Reported estimates of the global direct radiative effect (DRE) of BrC absorption range between +0.03 W/m² and +0.57 W/m²^{33,35}. This large range partly reflects the aforementioned large variation in BrC light-absorption properties, where different modeling studies have used different k_{BrC} values. To account for variability in k_{BrC} , experimental studies have developed parametrizations that correlated k_{BrC} in biomass-burning emissions with the BC-to-BrC ratio (BC/BrC) in the emissions^{11,23,36}. Specifically, as BC/BrC increases, BrC becomes more absorbing (i.e. k_{BrC} increases). The underlying reasoning is that a fraction of BrC is formed through the same route as BC, and as the combustion conditions become more conducive for BC formation, the light-absorption properties of the emitted BrC converge to those of BC³⁷.

Further complicating the representation of BrC in chemical transport models is that BrC absorption decays upon aging in the atmosphere. This process, referred to as photobleaching, involves the destruction of BrC chromophores due to either direct photolysis or photochemically induced reactions with OH^{26,38-41}. Atmospheric observations of the evolution of wildfire plumes have shown that BrC absorption decays with e-folding timescales on the order of 1 day^{29,42}. Wang et al.⁴³ implemented a photobleaching scheme in a chemical transport model and found that the global BrC absorption DRE dropped from +0.1 W/m² to 0.048 W/m² when they incorporated the effect of photobleaching. Similarly, Brown et al.⁴⁴ reported a global BrC absorption DRE of +0.13 W/m² and 0.06 W/m² with and without photobleaching, respectively. While the importance of light absorption by biomass-burning BrC has been established in experimental studies and atmospheric observations, the extent to which accounting for BrC absorption improves model performance is less clear.

1.3. Emissions from Gasoline Direct Injection (GDI) Vehicles

In 2012, the U.S. Environmental Protection Agency (EPA) and National Highway Traffic Safety Administration (NHTSA) put together coordinated programs with new standards for enhancing fuel economy and reducing CO₂ emissions of on-road vehicles⁴⁵. In response, the average real-world fuel economy of light-duty vehicles in the United States increased from 20 miles per gallon for model year 2005 to 24.9 miles per gallon for model year 2017 and the average CO₂ emissions decreased from 447 g/mile to 357 g/mile⁴⁶. Among the most prominent technologies adopted by car manufacturers to achieve these fuel-economy and CO₂ emissions goals is the gasoline direct injection (GDI) engine. Consequently, the market share of GDI-equipped vehicles increased from

2.3% in model year 2008 to 51% in model year 2018^{46,47}. EPA predicts a continued proliferation of GDI engines over the next decade, with a projected 93% of the United States fleet to be equipped with GDI engines by 2025⁴⁵.

Unlike the conventional port fuel injection (PFI) engines which mix fuel and air prior to injection into the engine cylinders, the GDI technology involves spraying the fuel directly into the cylinders, allowing for higher compression ratios⁴⁸. As a result, GDI engines achieve higher combustion efficiencies compared to their PFI counterparts, leading to the enhanced fuel economy and consequently, reduced CO₂ emissions. However, similar to diesel engines, the direct injection of fuel in GDI engines creates fuel-rich pockets near the injection zone. The combustion conditions in these pockets are conducive to formation of carbonaceous PM, especially BC^{49,50}. Consequently, GDI engines emit larger amounts of BC compared to PFI engines, as has been confirmed by several laboratory studies. Using a chassis dynamometer, Saliba et al.⁵¹ measured emissions from 82 light-duty vehicles (67 PFI, 15 GDI) with emission certification standards ranging from Tier 1 to SULEV (super ultra-low emission vehicle). They found that while BC emissions varied widely across vehicles, GDI vehicles emitted consistently higher levels of BC than PFI vehicles within each tier. Saliba et al.⁵¹ reported that on average, ULEV and SULEV (super / ultra-low emission vehicle) vehicles equipped with GDI engines emitted four-times more BC than PFI vehicles. Similar results were also reported by smaller scale chassis-dynamometer studies, yet with varying levels of enhancements, ranging between 3 and 50, in BC emissions of GDI relative to PFI vehicles⁵²⁻⁵⁹.

The evidence from these experimental studies indicates that the increase in BC emissions from GDI vehicles relative to PFI vehicles can offset the environmental and social

benefits associated with their improved fuel economy and reduced CO₂ emissions. This offset can occur on two levels. First, the increase in BC emissions directly impacts public health by contributing to an increase in ambient PM levels, thus imposing a social cost due to the known adverse health effects associated with PM^{3,60,61}. Even though BC emissions from gasoline vehicles contribute a small fraction of atmospheric PM, they are concentrated in regions with high population densities, thus magnifying their effect⁶. Second, BC is a strong absorber of solar radiation with a global-warming effect second only to CO₂^{8,9,62}. Therefore, the increase in BC emissions can counterbalance the climate benefits of the reduction in CO₂ emissions. While previous studies have reported net global climate benefits (i.e. global cooling) associated with shifting from PFI to GDI technologies^{51,63}, the net climate trade-off can be different on the regional scale, especially in regions with high vehicle densities. Due to the shorter lifetime of BC relative to CO₂ (days versus centuries⁶⁴), its warming effect is spatially localized and concentrated as opposed to CO₂ which has a globally uniform warming effect.

1.4. Objectives and Chapter Organization

This dissertation has two main objectives aimed at improving the understanding of the climate and public health impacts of combustion CAs over the U.S.. The first objective involves incorporating the effect of light-absorbing OA (BrC) emitted from wildland fires in the Weather Research and Forecasting model coupled with Chemistry (WRF-Chem)⁶⁵. Also using WRF-Chem as a modeling framework, the second objective is to estimate the aerosol-induced public health and direct radiative effects of shifting the U.S. gasoline light-duty vehicles fleet from PFI to GDI technology.

The dissertation is organized as follows: Chapter 2 presents a review of the implementation of BrC absorption in global climate models and highlights the associated challenges and uncertainties. Chapter 3 presents our approach of using parallel WRF-Chem simulations along with observational constraints to test the performance of BrC absorption parameterizations in a regional model over the U.S.. Chapter 4 presents our study in which we incorporated CA emission measurements from GDI vehicles into WRF-Chem in order to compare the air quality and climate impacts of emissions from GDI vehicles to traditional PFI vehicles. Chapter 5 presents concluding remarks from the two studies.

CHAPTER 2

REVIEW OF THE REPRESENTATION OF BROWN CARBON ABSORPTION IN CLIMATE MODELS

There are major uncertainties associated with the CA climate effects. The global average total radiative forcing (direct and indirect) of BC reported in the literature ranges over an order of magnitude, from +0.17 to +2.1 W/m² with a mean value of 1.1 W/m²⁸. Generally, models underestimate the absorption by aerosols. The ratio of model to observed aerosol absorption optical depth (AAOD) at 550 nm, varies regionally and ranges between 0.4 in higher latitudes of North America to 0.7 in Asia and South America⁶⁶. One of the potential reasons for the uncertainties is that solar radiation absorption by OA is often not accounted for in climate calculations. Many climate models define OA as an only scattering component⁶⁷. Some models use constant values for absorption (the wavelength-dependent imaginary part of refractive index, k)^{35,68,69} to account for the BrC effect, while laboratory and atmospheric measurements indicate a three-order of magnitude variability in k values^{11,70-73}. Recent studies have attempted to derive parameterizations for improving OA absorption representation. Saleh et al.¹¹ performed laboratory biomass-burning experiments and identified a correlation between the effective OA (BrC) absorption and the BC-to-OA ratio of the emissions. Since then, the BC-to-OA ratio has been confirmed to be a good predictor of carbonaceous aerosol light-absorption properties^{25,36}. In another study, aerosols single scattering albedo (SSA) was parameterized as a linear function of elemental to organic carbon ratio²⁵.

Furthermore, Cheng et al.⁷⁴ parameterized mass absorption cross-section (MAC), that is normalized absorption cross-section by absorbing component mass, and absorption Ångström exponent (AAE), that is absorption wavelength dependence, as a function of BC-to-OA ratio, based on controlled combustion experiments.

There has been attempts to apply such parameterizations in climate calculations. Saleh et al.⁷⁵ applied BrC absorption parameterization¹¹ to GEOS-Chem model simulations. They found that BrC absorption impact on global average DRE is +0.22 W/m² and +0.12 W/m², when aerosols are mixed externally and internally, respectively. In another study⁴³, two different BrC absorption parameterizations are used for primary and secondary OA separately. Furthermore, they accounted for the decay in BrC absorption (photobleaching) in the model by parameterizing photochemical aging of biomass-burning BrC. They compared model results with aircraft measurements over the U.S. and showed that most accurate model results are achieved when both BrC absorption and photobleaching effects are accounted for in the model. Also, they found that the mean global DRE for year 2014 is +0.048 W/m² that is about 30% of BC DRE⁴³. In a more recent study⁷⁶, Community Earth System Model (CESM) with a modified version of Community Atmosphere Model (CAM) was used to simulate BrC effect on climate in year 2010. They found that global average BrC DRE is +0.1 W/m² that is around 25% of BC DRE. However, the results also show that in some tropical regions, BrC DRE is higher than BC DRE.

Brown et al.⁴⁴ used CESM coupled with a modified CAM to calculate the BrC climate effects in the year 2003 to 2011. The results show that nine-year global average DRE of BrC is +0.13 W/m². They also found that implementing the BrC absorption

parameterization, described by Saleh et al.¹¹, resulted in an increase in AAE from model output and, therefore, a better agreement with Aerosol Robotic Network⁷⁷ (AERONET) observations. However, accounting for BrC absorption in CAM led to underestimating SSA compared to AERONET observations⁴⁴. Hammer et al.³³ calculated ultraviolet aerosol index (UVAI) using GEOS-Chem model and, also, retrieved UVAI from Ozone Monitoring Instrument (OMI) satellite data. Comparing satellite-retrieved and model-simulated UVAI, they found that the model has a large negative bias (-0.32 to -0.97) over biomass-burning regions such as South America and West Africa. However, accounting for BrC absorption in the model reduced this bias significantly. They also calculated annual mean all-sky DRE of BrC to be +0.03 W/m². June et al.⁷⁸ also used GEOS-Chem model to evaluate BrC absorption effect in the U.S. compared with Interagency Monitoring of Protected Visual Environments (IMPROVE) observations. They found that simulated AAOD agrees with those from IMPROVE observations within a factor of 2 when accounting for photobleaching effect. However, this factor is larger than 4 when ignoring photobleaching effect in the model. They also, calculated the global BrC DRE for 2016 to be +0.04 W/m²⁷⁸. In a more recent study, Brown et al.¹⁹ employed 12 observational datasets and nine global chemical transport models to evaluate biomass-burning aerosols absorptivity in the models. They found that many models overestimate absorption by biomass-burning aerosols and, therefore, underestimate SSA compared to observations over biomass-burning regions. They also reported that accounting for BrC absorption in the models exacerbated this underestimation¹⁹.

Overall, global climate-modeling studies show high uncertainties in the direct radiative effect of BrC absorption, with values ranging between +0.03 W/m² and +0.57 W/m²³¹.

Furthermore, there are conflicting results on whether including BrC absorption improves or worsens the comparison between models and observations over regions dominated by biomass burning emissions. In Chapter 3, we present a detailed investigation of representing BrC absorption in a regional climate model. The grid resolution in the regional model (12 km in our study) is finer than the global models (usually ranges from one to a few latitude/longitude degrees^{33,43,44,75}). This higher grid resolution provides a more precise model-observation comparison since a model output parameter in each grid cell is averaged over a smaller area compared with a global model. There has been attempts for high resolution global modeling but high computational cost is one of the main disadvantages⁷⁹⁻⁸¹. Therefore, a regional climate model allows for a better testing platform of BrC parameterizations. We chose a simulation period (August 2015) during which OA over the Western U.S. was dominated by high levels of BrC emitted from wildfires.

CHAPTER 3

OBSERVATIONALLY CONSTRAINED REPRESENTATION OF BROWN CARBON

EMISSIONS FROM WILDFIRES IN A CHEMICAL TRANSPORT MODEL¹

¹ Neyestani, S.E. and Saleh, R. 2021. To be submitted to *Environmental Science & Technology*.

Abstract

The month of August 2015 featured extensive wildfires in the Northwestern U.S. and no significant fires in Alaska and Canada. With the majority of carbonaceous aerosols (CA), including black carbon (BC) and brown carbon (BrC), over the U.S. dominated by emissions from these wildfires, this month presented a unique opportunity for testing wildfire BrC representation in the Weather Research and Forecasting model with chemistry (WRF-Chem). We performed parallel simulations that (1) did not account for BrC absorption, (2) accounted for BrC absorption, and (3) accounted for BrC absorption as well as its decay due to photobleaching. We used a comprehensive set of extensive and pseudo-intensive optical properties, namely the aerosol optical depth (AOD), aerosol absorption optical depth (AAOD), absorption Ångström exponent (AAE), and single scattering albedo (SSA) to constrain the model output against observations from the Aerosol Robotic Network (AERONET). We found that accounting for BrC absorption and photobleaching resulted in the best agreement with observations in terms of aerosol absorption (AAOD and AAE). However, the model severely underestimated AOD and SSA compared to observations. We attributed this discrepancy to missing scattering due to missing secondary organic aerosol (SOA) formation from wildfire emissions in the model. To test this hypothesis, we applied a zeroth-order representation of wildfire SOA, which significantly improved the AOD and SSA model-observation comparison. Our findings indicate that BrC absorption, the decay of its absorption due to photobleaching, as well as SOA formation should be accounted for in chemical transport models in order to accurately represent CA emissions from wildfires.

3.1. Introduction

Emissions from wildland fires are associated with significant impacts on public health¹²⁻¹⁴ and the climate^{15,16}. On the other hand, they play an essential ecological role that benefits natural resources and promotes ecosystem health and resilience^{17,18}. This tradeoff renders planning for the management and mitigation of wildland fires a major challenge¹⁸, especially due to the chaotic nature of open fires which makes model predictions of their public-health and climate impacts highly uncertain^{12,15,19}. Wildland fires encompass wildfires, which are usually ignited unintentionally, and prescribed fires¹⁸. On average in the U.S., prescribed fires (mostly in the Southeastern U.S.) and wildfires (mostly in the Western U.S.) cover similar burned areas annually of ~3 million ha each, though Western wildfires exhibit significant year-to-year variability¹² and have been increasing in intensity due to increase in global temperatures and drought episodes²⁰. With the continued decrease in anthropogenic emissions driven by emission standards and regulation²¹, the fraction of air pollutants attributed to wildland fires has been steadily increasing and is projected to continue to do so in the future²².

Wildland fires are major emitters of carbonaceous aerosol (CA), including organic aerosol (OA) and black carbon (BC). Numerous laboratory studies²³⁻²⁵ and field measurements²⁶⁻²⁸ have shown that OA from wildland fires is light-absorbing, and is categorized as brown carbon (BrC)²⁹⁻³¹. BC is a strong absorber of solar radiation with a positive radiative forcing that is globally second only to carbon dioxide^{8,9}. BrC is comprised of various species with a wide range of light-absorption properties, usually quantified using the imaginary part of the refractive index (k). On average, BrC emitted from biomass burning (including wildland fires) exhibits mid-visible k values that are one

to two orders of magnitude smaller than k of BC³¹. However, BrC emissions are usually one to two orders of magnitude larger than BC³², thus atmospheric BrC absorption is potentially equally important to BC. Furthermore, BrC exhibits absorption spectra that are largely skewed toward shorter visible and UV wavelengths, which can have important implications for photochemistry^{33,34}.

Representing BrC absorption in chemical transport models is challenging. Reported estimates of the global direct radiative effect (DRE) of BrC absorption range between +0.03 W/m² and +0.57 W/m²^{33,35}. This large range partly reflects the aforementioned large variation in BrC light-absorption properties, where different modeling studies have used different k_{BrC} values. To account for variability in k_{BrC} , experimental studies have developed parametrizations that correlated k_{BrC} in biomass-burning emissions with the BC-to-BrC ratio (BC/BrC) in the emissions^{11,23,36}. Specifically, as BC/BrC increases, BrC becomes more absorbing (i.e. k_{BrC} increases). The underlying reasoning is that a fraction of BrC is formed through the same route as BC, and as the combustion conditions become more conducive for BC formation, the light-absorption properties of the emitted BrC converge to those of BC³⁷.

Further complicating the representation of BrC in chemical transport models is that BrC absorption decays upon aging in the atmosphere. This process, referred to as photobleaching, involves the destruction of BrC chromophores due to either direct photolysis or photochemically induced reactions with OH^{26,38-41}. Atmospheric observations of the evolution of wildfire plumes have shown that BrC absorption decays with e-folding timescales on the order of 1 day^{29,42}. Wang et al.⁴³ implemented a photobleaching scheme in a chemical transport model and found that the global BrC

absorption DRE dropped from $+0.1 \text{ W/m}^2$ to 0.048 W/m^2 when they incorporated the effect of photobleaching. Similarly, Brown et al.⁴⁴ reported a global BrC absorption DRE of $+0.13 \text{ W/m}^2$ and 0.06 W/m^2 with and without photobleaching, respectively.

While the importance of light absorption by biomass-burning BrC has been established in experimental studies and atmospheric observations, the extent to which accounting for BrC absorption improves model performance is less clear. On one hand, several investigations have reported that accounting for BrC absorption resulted in better agreement between models and observations. Hammer et al.³³ compared ultraviolet aerosol index (UVAI) values retrieved from Ozone Monitoring Instrument (OMI) data and those simulated by a global climate model and found that ignoring BrC absorption in the model caused a negative bias in UVAI over biomass-burning regions³³. Wang et al.⁴³ used aircraft measurements over the U.S. to constrain model-simulated BrC absorption. They found that best model-measurement agreement was achieved by accounting for both BrC absorption and photobleaching. Similarly, June et al.⁷⁸ found that ignoring photobleaching in a global chemical transport model led to overestimating absorption aerosol optical depth (AAOD) compared to Interagency Monitoring of Protected Visual Environments (IMPROVE) observations. On the other hand, Brown et al.⁴⁴ found that even though implementing BrC absorption in a global chemical transport model led to better agreement between model AAE over biomass-burning regions and those retrieved from Aerosol Robotic Network (AERONET) observations, the model underestimated single scattering albedos (SSA) over biomass-burning regions compared to AERONET. This finding was confirmed by a more comprehensive follow-up study which reported that all of 9 global models underestimated SSA over biomass-burning regions compared

to measurements from 12 observational data sets¹⁹. Indeed, that study reported that accounting for BrC absorption exacerbated the underestimation of SSA.

Here, we present a detailed investigation of the extent to which representing absorption by BrC from wildfire emissions in a chemical transport model improves the comparison with remote-sensing observations. Using the Weather Research and Forecasting model with chemistry (WRF-Chem)⁸², we performed simulations for the month of August 2015 over the U.S. where we treated OA emissions from wildfires as (1) non-absorbing, (2) absorbing (i.e. BrC), and (3) BrC with evolving light-absorption properties due to photobleaching. We then applied a comprehensive set of constraints retrieved from AERONET observations to assess the model performance for each treatment. The constraints included both extensive (AOD and AAOD) and pseudo-intensive (AAE and SSA) optical properties.

3.2. Experimental Design

The goal of this study is to assess the importance of accounting for the absorption of BrC in wildfire CA emissions for accurately representing their interaction with solar radiation. To that end, we performed a series of WRF-Chem simulations over the U.S. for the month of August 2015. We chose this month because it featured extensive wildfire events in the Northwestern U.S., while no major fires were recorded in Alaska and Canada. Therefore, this simulation period presents a unique test case with high levels of wildfire CA emissions within the simulation domain and minimal transport from outside the domain boundaries. Over the month of August 2015, approximately 93% of the CA emissions were from biomass burning (7% were from anthropogenic sources), 92% of which were from the Northwestern wildfires. The impact of the CA emissions from the

high wildfire activity is depicted in Figure 3.1a, where the modeled monthly average wildfire CA column burden exceeded 50 mg/m^2 over the Northwestern U.S.. Figure 3.1b shows the fraction of CA column burden over the U.S. attributed to the wildfire emissions. CA from wildfire emissions dominated the CA column burden over the majority of the U.S. regions. The contribution of the Northwestern wildfires to CA is the lowest in the Eastern U.S. due to both the long transport distance as well as the relatively high levels of anthropogenic CA emissions and biogenic secondary organic aerosol (SOA) formation over that region.

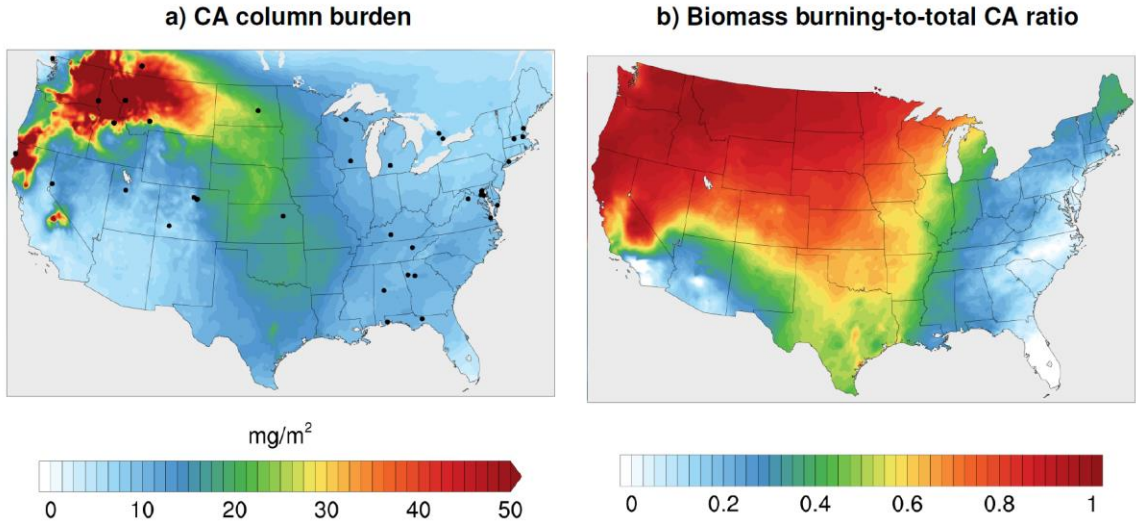


Figure 3.1. (a) Column burden of carbonaceous aerosol attributed to biomass-burning emissions averaged over the month of August 2015. As evident in the spatial distribution, emissions from Northwestern wildfires constitute the majority of biomass-burning emissions in the simulation period. Black dots show the locations of AERONET stations used in the model-observation comparisons. (b) The fraction of carbonaceous-aerosol column burden attributed to biomass-burning (wildfire) emissions.

In order to assess the impact of representing BrC in wildfire emissions on CA optical properties, we performed 4 parallel simulations:

1. Base: We treated all OA emissions, including biomass-burning OA, as non-absorbing. This is the default setting in WRF-Chem.
2. BrC: We treated biomass-burning OA emissions as BrC based on the parameterization of Saleh et al.¹¹, as further elaborated below. Since more than 90% of biomass-burning OA emissions are attributed to Northwestern wildfires in this simulation period, biomass-burning BrC is effectively wildfire BrC. We note that anthropogenic OA emissions as well as SOA from all precursors (biogenic, anthropogenic, and biomass burning) were treated as non-absorbing.
3. BrC+bleaching: We accounted for decay in BrC absorption due to photobleaching based on the parameterization of Wang et al.⁴³, as further elaborated below.
4. BrC+bleaching+SOA: We incorporated a zeroth-order representation of SOA formation from the oxidation of vapors in wildfire emissions.

3.3. Model Description

We employed WRF-Chem⁸² version 3.8. We set a single domain encompassing the contiguous U.S. with a horizontal resolution of 12 km (396×246 grid cells) and 30 pressure-based vertical layers extending up to 50 hPa. The model time step was 60 seconds and the output was saved as 3-hour averages. A 10-day spin-up time was added at the start of the simulation period. The initial and boundary conditions were processed for meteorology calculations using the National Center for Environmental Prediction (NCEP) final reanalysis data with a horizontal resolution of $1^\circ \times 1^\circ$ and temporal resolution of 6 hours⁸³. We also implemented the reanalysis data to apply Four-

Dimensional Data Assimilation (FDDA) nudging⁸⁴ to the wind and temperature components in the simulations.

We obtained both anthropogenic and biomass-burning emissions data from the EPA National Emission Inventory (NEI)⁸⁵. In addition to satellite fire detection, wildland-fire emissions in NEI are obtained from fire information databases reported by national, regional, state, local, and tribal agencies⁸⁶. We preprocessed the NEI emissions for use in WRF-Chem using the Sparse Matrix Operator Kernel Emission (SMOKE)⁸⁷ model version 3.6.5 and converted the SMOKE hourly emission output into WRF-Chem compatible input files using EPA_ANTHRO_EMIS code developed by NCAR⁸⁸. For computational efficiency, a simplified plume rise method⁸⁹ was applied to the fire emission sources before using as input in WRF-Chem.

Gas-phase chemistry was processed using the Model for Ozone and Related Chemical Tracers (MOZART)⁹⁰. Model of Emissions of Gases and Aerosols from Nature (MEGAN) version 2⁹¹ was used to calculate biogenic emissions online with meteorology. The Model for Simulating Aerosol Interactions and Chemistry (MOSAIC)⁹², which includes major aerosol species such as BC, organic carbon (OC), sulfate, nitrate, and ammonium, were selected for simulating aerosol microphysics.

Within MOSAIC, gas-particle partitioning of semi-volatile organic species and inorganic aerosol thermodynamics are simulated based on the volatility basis set framework⁹³ and the multi-component equilibrium solver over aerosols⁹⁴, respectively. Also, we represented SOA formation in the model using a simplified parameterization described by Hodzic and Jimenez⁹⁵, where a precursor organic gas is oxidized to form SOA. The

emission rate of the precursor organic gas is proportional to CO emission rate that is based on SOA-to-CO concentration ratio from observations⁹⁵.

WRF-Chem employs Mie theory to perform aerosol optical calculations (scattering coefficients and absorption coefficients) using MOSAIC size distributions and the complex refractive indices associated with each MOSAIC chemical constituent⁶⁷. We used the model default complex refractive indices except for wildfire BrC, which was parameterized as described in the next section. We employed an external mixing assumption for BC, and all the other aerosol components were treated as well-mixed within each size bin. We note that WRF-Chem does not provide this mixing state as an option. Therefore, we defined new (duplicate) size bins for BC particles which were only employed for optical calculations in the optical module and thus did not affect the aerosol microphysical and chemical processes in the chemical transport module.

3.4. Brown Carbon Parameterization

In its default configuration, WRF-Chem treats OA from all sources, including wildfires, as non-absorbing by assigning an OA imaginary part of a refractive index (k_{OA}) of zero. In simulations 2, 3, and 4 (described above), we accounted for absorption by biomass-burning (mostly wildfire) OA, i.e. we treated wildfire OA as BrC. We applied the parameterization of Saleh et al.¹¹, which calculates k_{BrC} of biomass-burning emissions as a function of the BC-to-BrC ratio (BC/BrC) in the emissions:

$$k_{BrC,550} = 0.016 \times \log(BC/BrC) + 0.03925 \quad (3.1)$$

$$w = \frac{0.2081}{BC/BrC + 0.0699} \quad (3.2)$$

Where $k_{\text{BrC},550}$ is k_{BrC} at 550 nm and w is the wavelength dependence. k_{BrC} at other wavelengths is calculated as:

$$k_{\text{BrC},\lambda} = k_{\text{BrC},550} \times \left(\frac{550}{\lambda} \right)^w \quad (3.3)$$

According to this parameterization, $k_{\text{BrC},550}$ increases while w decreases with increasing BC/BrC, signifying that the BrC absorption becomes stronger but has a flatter wavelength dependence. The inverse relationship between $k_{\text{BrC},550}$ and w has been observed in several studies^{23,36,96}. It is noteworthy that BC has $w = 0$ in the visible spectrum.

We note that in Equations 3.1 and 3.2, BC refers to biomass-burning BC and BrC refers to biomass-burning OA. Therefore, in order to implement the parameterization (Equations 3.1 and 3.2) in WRF-Chem, we defined new species to separate the OA emissions into anthropogenic OA and biomass-burning OA (BrC) and the BC emissions into anthropogenic BC and biomass-burning BC.

In simulations 3 and 4 (described above), we accounted for the decay in BrC absorption upon aging in the atmosphere due to photobleaching^{26,38-41} based on the parameterization of Wang et al.⁴³. That study assumed that BrC absorption decreased following a first-order dynamic response with a time constant (i.e. lifetime) of approximately 1 day^{29,42} at an OH concentration of 5×10^5 molecules/cm³. Therefore, k_{BrC} at each time step can be calculated as:

$$k_{\text{BrC},t+\Delta t} = k_{\text{BrC},t} \exp\left(-\frac{[\text{OH}] \Delta t}{5 \times 10^5}\right) \quad (3.4)$$

Where Δt is model time step in days and $[\text{OH}]$ is OH concentration in molecules/cm³.

Following Wang et al.⁴³, we did not allow k_{BrC} to drop below 1/4 of the original value (at $t = 0$), which is consistent with atmospheric observations that the decay in absorption associated with photobleaching plateaus at a certain threshold^{29,42}.

Figure A1a in the appendix A shows the spatial distribution of $[\text{OH}]$ predicted by WRF-Chem for the month of August 2015, averaged over the first 8 layers of the model (where BrC effect is important). The corresponding BrC absorption half-lives, estimated from Equation 3.4, are shown in Figure A1b. The domain-average BrC absorption half-life was 0.52 days, which is consistent with the global-average half-life of 0.59 days reported by Brown et al.⁴⁴.

3.5. Observational Constraints

In order to assess the optical treatments of BrC, we compared the model output with observations from the AERONET observations⁷⁷. Figure 3.1 shows the locations of AERONET stations (black dots) used in this study.

The model-observation comparisons included both extensive optical properties, namely the aerosol absorption optical depth (AAOD, Figure 3.2) and aerosol optical depth (AOD, Figure 3.3), as well as pseudo-intensive optical properties, namely the absorption Ångström exponent (AAE, Figure 3.4) and the single scattering albedo (SSA, Figure 3.5). We note that even though AAE and SSA do not depend on aerosol concentration, they are not fundamental intensive optical properties (like for example, the complex refractive index) as they depend on particle size and mixing state of the aerosol.

AERONET inversion products use an inversion algorithm described in Dubovik & King⁹⁷ where radiative transfer forward modeling is coupled with statistical estimation and priori constraints to optimize the inversion method. AERONET inversion products have two quality assurance levels⁹⁸. The first level (1.5) includes thresholds on azimuth and scattering angles while the second level (2.0) applies an extra set of criteria (e.g. omitting data points with AODs smaller than 0.4). For this study, we used level 1.5 AERONET inversion data to retain a large number of data points for comparison with the model results.

AERONET observations are reported at 440 nm, 675 nm, 870 nm, and 1020 nm. For the AAOD, AOD, and SSA comparisons, we focus on the observations at 440 nm, where BrC absorption is the strongest. Comparisons at 675 nm are shown in Figures A2-A5 in the ESI.

We calculated AAE from AERONET AAOD at 440 nm and 675 nm as:

$$AAE = \frac{\log\left(\frac{AAOD_{440}}{AAOD_{675}}\right)}{\log\left(\frac{675}{440}\right)} \quad (3.5)$$

WRF-Chem optical properties are calculated at 300 nm, 400 nm, 600 nm, and 999 nm). Therefore, we converted WRF-Chem AAOD, AOD, and SSA values to 440 nm for comparison with AERONET observations. First, we calculated AAE and the extinction Ångström exponent (EAE) from WRF-Chem AAOD and AOD at 400 nm and 600 nm as:

$$AAE = \frac{\log\left(\frac{AAOD_{400}}{AAOD_{600}}\right)}{\log\left(\frac{600}{400}\right)} \quad (3.6)$$

$$EAE = \frac{\log\left(\frac{AOD_{400}}{AOD_{600}}\right)}{\log\left(\frac{600}{400}\right)} \quad (3.7)$$

Then, we calculated AAOD and AOD at 440 nm as:

$$AAOD_{440} = AAOD_{400} \times \left(\frac{400}{440}\right)^{AAE} \quad (3.8)$$

$$AOD_{440} = AOD_{400} \times \left(\frac{400}{440}\right)^{EAE} \quad (3.9)$$

3.6. Model-Observation Comparison

3.6.1. The Base Simulation

As shown in Figure 3.2a, the slope of the linear fit to model AAOD versus AERONET AAOD at 440 nm is 0.49 for the Base simulation. This underestimation of aerosol absorption at 440 nm by approximately a factor of 2 on average is an indication of missing BrC absorption in the Base simulation. The effect of missing BrC absorption in the model is more evident in the AAE comparison (Figure 3.4a). AERONET AAE values range between 0.8 and 1.4, which is consistent with variable contributions of BC and BrC to absorption, where smaller AAE values indicate BC-dominated absorption and larger AAE values indicate and increased contribution to absorption by BrC. On the other

hand, the model AAE values exhibit a narrow range between 0.6 and 0.7 and no correlation with AERONET AAE because absorption in the Base simulation is solely dictated by BC.

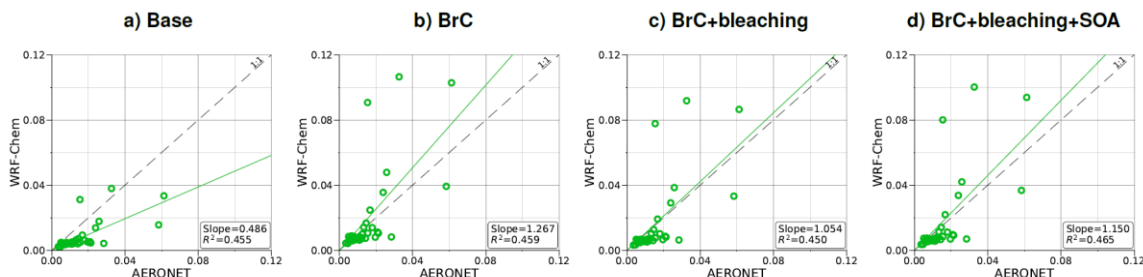


Figure 3.2. Comparison between monthly average AAOD at 440 nm for August 2015 obtained from AERONET observations and WRF-Chem output with four different model treatments of wildfire carbonaceous aerosol emissions.

The slope of model AOD versus AERONET AOD is 0.31 (Figure 3.3a), which is smaller than the slope of the AAOD comparison. This indicates that in addition to the underestimation in aerosol absorption in the model, there is a more significant underestimation in scattering. As expected, because scattering is more underestimated on average than absorption in the model, a substantial fraction of model SSA values are smaller than AERONET SSA (Figure 3.5a). The model SSA values are generally clustered in two groups, one in good agreement with AERONET and one lower than AERONET. This clustering can be understood by examining the spatial distribution of model and AERONET SSA in Figure 3.6. The model SSA values are smallest in the Northwest, and increase toward the South and East, with the largest values along the Eastern region. The AERONET observations are mostly clustered in the Western region (where model SSA is smallest) and the Eastern region (where model SSA is the largest and closest to AERONET SSA), thus creating the two clusters in Figure 3.5a. More

importantly, comparing the spatial distributions of SSA (Figure 3.6) and wildfire CA column burden (Figure 3.1b) clearly indicates that the underestimation in model SSA (i.e. underestimation in aerosol scattering) is associated with the treatment of wildfire CA in the model. The missing wildfire CA scattering is further explored later in this section.

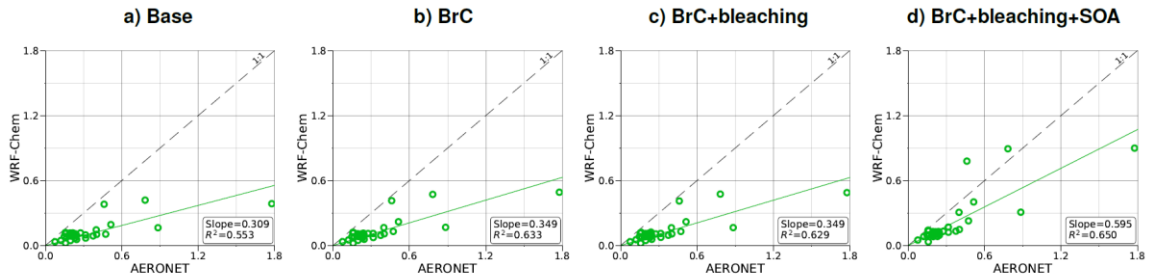


Figure 3.3. Comparison between monthly average AOD at 440 nm for August 2015 obtained from AERONET observations and WRF-Chem output with four different model treatments of wildfire carbonaceous aerosol emissions.

3.6.2. Effect of Incorporating Carbon Absorption

Model AAOD values in the BrC simulation are significantly larger than in the Base simulation. As shown in Figure 3.2b, the slope of model AAOD versus AERONET AAOD for the BrC simulation is 1.23. The BrC simulation exhibits an improved model-observation AAOD comparison compared to the Base simulation (slope = 0.49; Figure 3.2a), though incorporating BrC absorption leads to overestimating AAOD, on average. This is further evidenced in the AAE comparison. As shown in Figure 3.4b, model AAE in the BrC simulation is better correlated with AERONET AAE compared to the Base simulation. However, almost all model AAE values are larger than AERONET AAE values. Overall, even though representing BrC based on the parameterization of Saleh et al.¹¹ leads to overestimating aerosol absorption, it presents an improvement in the

prediction of aerosol absorption compared to the Base simulation, where BrC is neglected.

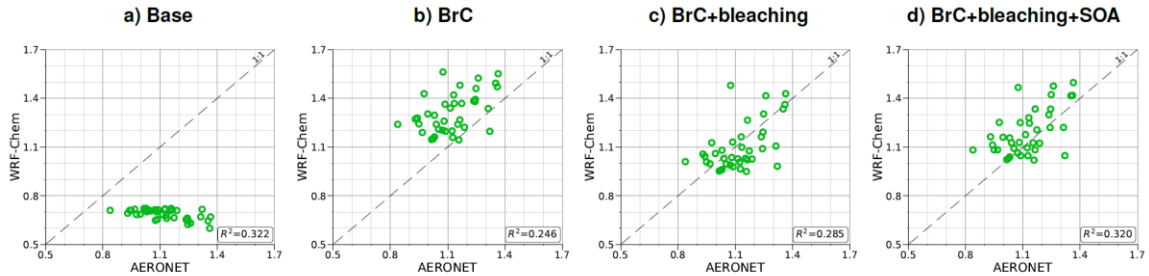


Figure 3.4. Comparison between monthly average AAE for August 2015 obtained from AERONET observations and WRF-Chem output with four different model treatments of wildfire carbonaceous aerosol emissions.

BrC absorption has a negligible effect on aerosol scattering and only affects the absorption component of aerosol extinction. Consequently, incorporating BrC absorption has only a small effect on the AOD model-observation comparison, as evident in comparing Figure 3.3a and Figure 3.3b. Because BrC absorption causes a substantial increase in absorption and negligible effect on scattering, this is reflected in a substantial decrease in SSA in the BrC simulation compared to the Base simulation. As shown in Figure 3.5b, incorporating BrC absorption widens the gap between the two clusters described above and substantially worsens the SSA model-observation comparison. As expected, accounting for the decay in BrC absorption due to photobleaching (BrC+bleaching simulation) leads to a reduction in both AAOD and AAE compared to the BrC simulation. As shown in Figure 3.2c and Figure 3.4c, the AAOD and AAE in the BrC+bleaching simulation exhibit a very good agreement with AERONET observations. However, similar to the Base and BrC simulation, the BrC+bleaching simulation severely underestimates aerosol scattering as evident in the model-observation AOD comparison

(Figure 3.3c). Because incorporating photobleaching reduces BrC absorption, the SSA values in the BrC+bleaching simulation (Figure 3.5c) are larger than in the BrC simulation (Figure 3.5b) resulting in a slight improvement in the SSA model-observation comparison. However, SSA model-observation comparison in the BrC+bleaching simulation is still worse than the Base simulation (Figure 3.5a).

To recap, neglecting BrC absorption (Base simulation) results in a significant underestimation of aerosol absorption as evidenced in the model-observation AAOD and AAE comparisons. Accounting for BrC absorption (BrC simulation) leads to overestimating AAOD and AAE, but results in a better comparison with observation. The best agreement in AAOD and AAE with observations is achieved when accounting for both BrC absorption and photobleaching (BrC+bleaching simulation). On the hand, all simulations severely underestimate scattering compared to observations, as evident in the AOD comparisons. We note that the better model-observation agreement of SSA in the Base simulation compared to the BrC and BrC+bleaching simulations is rather serendipitous; it is due to the fact that the Base simulation underestimates both absorption and scattering.

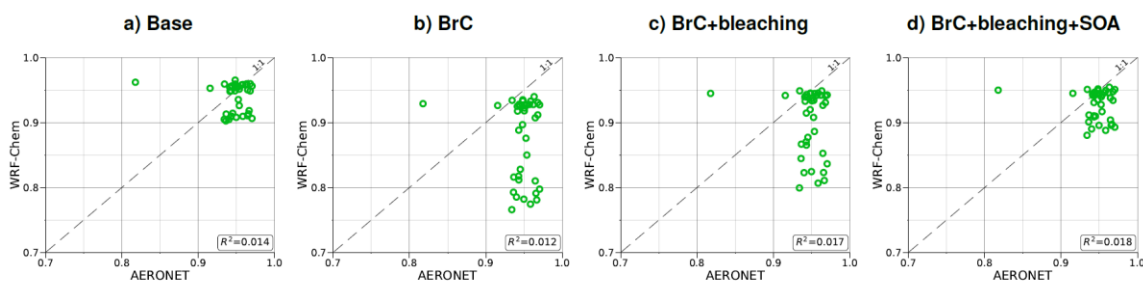


Figure 3.5. Comparison between monthly average SSA at 440 nm for August 2015 obtained from AERONET observations and WRF-Chem output with four different model treatments of wildfire carbonaceous aerosol emissions.

3.6.3. The Missing Scattering

The model-observation comparisons employed in this study (Figure 3.2, 3.3, 3.4, and 3.5) include both absorption and scattering, as well as extensive and pseudo-intensive properties. This comprehensive set of constraints enables dissecting the missing scattering problem described in the previous sub-section. For instance, the underestimation of AOD cannot be explained by an underestimation in wildfire CA emissions. Reconciling model and AERONET AODs would require increasing CA emissions by a factor of ~ 3 (Figure 3.3), which would lead to overestimating AAOD (Figure 3.2). The underestimation of AOD cannot be explained by wrong BC/BrC or BrC optical properties either. Increasing the amount of BrC (or making BrC more absorbing and/or scattering) to reconcile the model and AERONET AOD would lead to either overestimating AAE, or AAOD, or both.

A plausible explanation that satisfies the observational constraints is that the model misses SOA formation from wildfire emissions. Laboratory experiments⁹⁹⁻¹⁰² and field measurements¹⁰³⁻¹⁰⁵ have reported SOA formation from the oxidation of vapor precursors in wildfire emissions, though to highly variable extents. We performed a simulation (BrC+bleaching+SOA) that involves a zeroth-order representation of wildfire SOA in addition to representing BrC and photobleaching. We treated SOA formation as direct emissions from wildfires alongside BrC (i.e. primary organic aerosol; POA) and BC. We assumed equal amounts of SOA and POA, which is within the range of values reported in the literature¹⁰². For simplicity, we treated wildfire SOA as non-absorbing. Figure 3.7a shows monthly average SOA column burdens over the model domain from the Base simulation. The relatively high levels of SOA over the Eastern U.S. are due to biogenic

volatile organic compounds (VOCs) emissions, which are efficient SOA precursors. On the other hand, SOA formation from VOCs and other precursors (intermediate volatility and semi-volatile organic compounds)¹⁰⁶ in wildfire emissions is missing in the model as evidenced by the low SOA levels in the Northwest. Incorporating BrC leads to a slight decrease in SOA concentrations (Figure 3.6b and 6c) because BrC light absorption reduces the surface temperature slightly, which leads to a reduction in emission rates of biogenic VOCs⁹¹. Representing wildfire SOA in the model (BrC+bleaching+SOA simulation) increases SOA column burden by about two orders of magnitudes over the wildfire regions in the Northwest (Figure 3.7d).

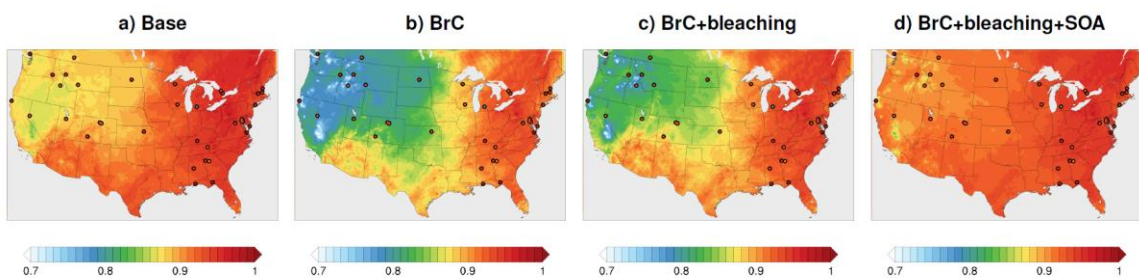


Figure 3.6. The SSA at 440 nm averaged over the month of August 2015 from WRF-Chem output with four different model treatments of wildfire carbonaceous aerosol emissions. The color dots show the locations and SSA values of AERONET stations used in the model-observation comparisons.

Relative to the BrC+bleaching simulation, accounting for SOA formation in the BrC+bleaching+SOA simulation has a small effect on AAOD as shown in Figure 3.2c and 2d (slope of AAOD comparison increases from 1.05 to 1.15) and AAE (Figure 3.4c and 4d). However, accounting for SOA formation has a significant effect on AOD as shown in Figure 3.3c and 3d (slope of AOD comparison increases from 0.35 to 0.60), thus largely reconciling the model SSA and AERONET SSA (Figure 3.5d). Brown et

al.¹⁹ performed a comprehensive SSA comparison between 9 global chemical transport / Earth system models and 12 observational data sets over globally distributed regions dominated by biomass-burning emissions. That study found that all models underestimated SSA compared to observations. Since those models did not include SOA formation from biomass-burning emissions¹⁹, it is plausible that the underestimated scattering due to the missing SOA at least partly explains the inconsistency between the models and the observations.

The results obtained from the model-observation comparison performed in this study indicate that SOA formation from precursors in wildfire emissions is important and should be accounted for in chemical transport models. This SOA has implications not only to the radiative balance in the atmosphere, but, perhaps to a larger extent, to air quality (public health). Neglecting wildfire SOA can lead to severely underestimating aerosol surface concentrations, thus exposure, in regions impacted by wildfire emissions.

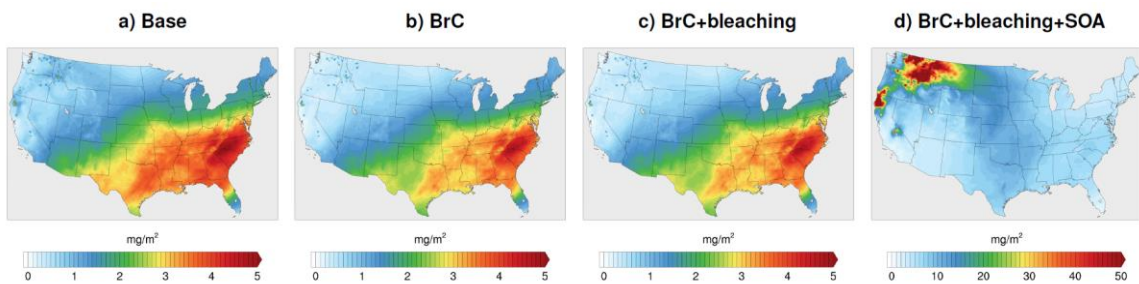


Figure 3.7. Column burden of SOA averaged over the month of August 2015 from WRF-Chem output with four different model treatments of wildfire carbonaceous aerosol emissions.

3.7. Conclusions

In this study, we employed a comprehensive set of optical properties retrieved from AERONET observations as complementary constraints for testing the

representation of wildfire BrC in WRF-Chem. Specifically, the combination of AAOD (an extensive aerosol light-absorption property) and AAE (a pseudo-intensive light-absorption property that describes the wavelength dependence of absorption) comparisons showed that BrC absorption should be accounted for in order to reconcile model and observed absorption. One could match model and observed AAOD at a certain wavelength by scaling wildfire BC emissions, but that would lead to disagreement at other wavelengths if BrC absorption was ignored. Overall, the best model-observation agreement in terms of aerosol absorption was achieved by representing wildfire BrC absorption using the parameterization of Saleh et al.¹¹ and its decay by photobleaching using the parameterization of Wang et al.⁴³. However, in order to also reconcile model and observed AOD and SSA, we found that the model should account for relatively high levels of wildfire SOA (similar levels to wildfire POA). Neglecting wildfire SOA results in severely underestimating aerosol scattering. This finding indicates that modeling frameworks that do not account for wildfire SOA underestimate exposure to aerosols in regions impacted by wildfire emissions.

CHAPTER 4

DIRECT RADIATIVE EFFECT AND PUBLIC HEALTH IMPLICATIONS OF AEROSOL EMISSIONS ASSOCIATED WITH SHIFTING TO GASOLINE DIRECT- INJECTION (GDI) TECHNOLOGIES IN LIGHT-DUTY VEHICLES IN THE UNITED STATES¹

¹ Neyestani, S.E. et al. 2020. *Environmental Science and Technology*. 54:687-696
Reprinted here with permission of the publisher.

Abstract

Due to their enhanced fuel economy, the market share of gasoline direct-injection (GDI) vehicles has increased significantly over the past decade. However, GDI engines emit higher levels of black carbon (BC) aerosols compared to the traditional port-fuel injection (PFI) engines. Here, we performed coupled chemical-transport and radiative-transfer simulations to estimate the aerosol-induced public-health and direct radiative effects of shifting the U.S. fleet from PFI to GDI technology. By comparing simulations with current emission profiles and emission profiles modified to reflect a shift from PFI to GDI, we calculated the change in aerosol (mostly BC) concentrations associated with the fleet change. Standard concentration-response calculations indicated that the total annual deaths in the U.S. attributed to particulate gasoline-vehicle emissions would increase from 855 to 1599 due to shifting from PFI to GDI. Furthermore, the increase in BC associated with the shift would lead to an annual-average positive radiative effect over the U.S. of approximately $+0.075 \text{ W/m}^2$, with values as large as $+0.45 \text{ W/m}^2$ over urban regions. On the other hand, the reduction in CO_2 emissions associated with the enhanced fuel economy of GDI vehicles would yield a globally uniform negative radiative effect, estimated to be -0.013 W/m^2 over a 20-year time horizon. Therefore, the climate burden of the increase in BC emissions dominates over the U.S., especially over source regions.

4.1. Introduction

In 2012, the U.S. Environmental Protection Agency (EPA) and National Highway Traffic Safety Administration (NHTSA) put together coordinated programs with new

standards for enhancing fuel economy and reducing CO₂ emissions of on-road vehicles⁴⁵. In response, the average real-world fuel economy of new light-duty vehicles sold in the United States increased from 20 miles per gallon for model year 2005 to 24.9 miles per gallon for model year 2017 and the average CO₂ emissions decreased from 447 g/mile to 357 g/mile⁴⁶. Among the most prominent technologies adopted by car manufacturers to achieve these fuel-economy and CO₂ emissions goals is the gasoline direct injection (GDI) engine. Consequently, the market share of GDI-equipped vehicles increased from 2.3% in model year 2008 to 51% in model year 2018^{46,47}. EPA predicts a continued proliferation of GDI engines over the next decade, with a projected 93% of the United States fleet to be equipped with GDI engines by 2025⁴⁵.

Unlike the conventional port fuel injection (PFI) engines which mix fuel and air prior to injection into the engine cylinders, the GDI technology involves spraying the fuel directly into the cylinders, allowing for higher compression ratios⁴⁸. As a result, GDI engines achieve higher combustion efficiencies compared to their PFI counterparts, leading to the enhanced fuel economy and consequently, reduced CO₂ emissions by up to 14%¹⁰⁷. However, similar to diesel engines, the direct injection of fuel in GDI engines creates fuel-rich pockets near the injection zone, and the combustion conditions in these pockets are conducive to formation of carbonaceous particulate matter (PM), especially black carbon (BC)^{49,50}. Consequently, GDI engines emit larger amounts of BC compared to PFI engines, as has been confirmed by several laboratory studies. Using a chassis dynamometer, Saliba et al.⁵¹ measured emissions from 82 light-duty vehicles (67 PFI, 15 GDI) with emission certification standards ranging from Tier 1 to SULEV (super ultra-low emission vehicle). That study found that while BC emissions varied widely across vehicles, GDI vehicles

emitted consistently higher levels of BC than PFI vehicles within each tier. Saliba et al.⁵¹ reported that on average, ULEV and SULEV (super / ultra-low emission vehicle) vehicles equipped with GDI engines emitted approximately four-times more BC than PFI vehicles and similar levels of organic carbon (OC). Enhancement in BC emissions of GDI relative to PFI vehicles was also reported by smaller scale chassis-dynamometer studies⁵²⁻⁵⁹, yet with varying levels of enhancements, ranging between 3 and 50.

The significant increase in BC emissions in GDI vehicles relative to PFI vehicles can offset the social benefits associated with their improved fuel economy and reduced CO₂ emissions. This offset can occur via two processes. First, the increase in BC emissions directly impacts public health by contributing to an increase in ambient PM_{2.5} (particulate matter with diameters smaller than 2.5 μm) levels, thus imposing a social cost due to the known adverse health effects associated with PM_{2.5}^{3,60,61}. Even though BC emissions from gasoline vehicles contribute a small fraction of atmospheric PM_{2.5}, they are concentrated in regions with high population densities, thus magnifying their effect⁶. Second, BC is a strong absorber of solar radiation with a global-warming effect second only to CO₂^{8,9,62}. Therefore, the increase in BC emissions can counterbalance the climate benefits of the reduction in CO₂ emissions. Previous studies reported net global-mean climate benefits (i.e. net global-mean negative radiative effect) associated with shifting from PFI to GDI technologies using the global-warming potential (GWP) framework^{51,63}. GWP compares the total energy absorbed by a pollutant (in this case BC) versus CO₂ over a certain time horizon, and is, by definition, on a global scale. However, the net climate trade-off can be different on the regional scale, especially in regions with high vehicle densities. Due to the shorter lifetime of BC relative to CO₂ (days versus centuries⁶⁴), its radiative effect is

spatially localized and concentrated as opposed to CO₂ which has a globally uniform radiative effect¹⁰⁸.

In this paper, we explore the public-health and climate impacts of a large-scale shift in vehicle engine technology from PFI to GDI in the United States. We used a regional coupled chemical-transport / radiative-transfer model to estimate spatially resolved changes in aerosol (mainly BC) concentrations and the associated direct radiative effect (DRE). We also applied standard concentration-response calculations to predict spatially resolved premature mortality rates induced by the increased aerosol (PM_{2.5}) exposure.

4.2. Methods

4.2.1. Model Description

We used the Weather Research and Forecasting model with chemistry (WRF-Chem)⁸² version 3.8, which performs coupled meteorology, chemical-transport and radiative-transfer calculations. WRF-Chem was configured with a single domain covering the contiguous U.S. (approximately 25.1° to 52.8° N and -123.9° to -70.1° W), a horizontal resolution of 12 km (400 × 260 horizontal grid cells) , and 30 vertical layers extending up to 20 km above the surface. The temporal resolution for integrating the governing equations (i.e., model timestep) was 60 seconds and output was saved as 3 hourly averages. Meteorological initial and boundary conditions were obtained from the National Center for Environmental Prediction (NCEP) final reanalysis data with horizontal resolution of 1° × 1° and temporal resolution of 6 hours⁸³. We also used the reanalysis data to apply Four-Dimensional Data Assimilation (FDDA) nudging⁸⁴ to the wind components in the simulations to improve model validation against observations and comparison between different simulations.

We obtained anthropogenic emissions data from the EPA National Emission Inventory 2011 (NEI-2011)⁸⁵ and preprocessed it for use in WRF-Chem using the Sparse Matrix Operator Kernel Emission (SMOKE)⁸⁷ model version 3.6.5. Finally, we converted the SMOKE output into a format (NetCDF) readable by WRF-Chem using a FORTRAN code developed by NCAR⁸⁸. Gas-phase chemistry was simulated using the Model for Ozone and Related Chemical Tracers (MOZART)⁹⁰, which includes 85 species, 39 photolysis reactions, and 157 chemical reactions⁹⁰. Aerosol microphysics was simulated using the Model for Simulating Aerosol Interactions and Chemistry (MOSAIC)⁹², which explicitly tracks major aerosol species such as BC, organic carbon (OC), sulfate, nitrate, and ammonium in eight size bins. MOSAIC simulates gas-particle partitioning of semi-volatile organic species based on the volatility basis set framework⁹³ and inorganic aerosol thermodynamics based on the multi-component equilibrium solver over aerosols⁹⁴. The formation of secondary organic aerosols (SOA) was simulated using the parameterization described in Hodzic & Jimenez⁹⁵.

WRF-Chem simulates the direct radiative effect of aerosols, online, using the Rapid Radiative Transfer Model - Global (RRTMG) scheme¹⁰⁹. The extensive aerosol optical properties (scattering coefficients, absorption coefficients, and asymmetry parameters) required for the radiative-transfer calculations were calculated based on MOSAIC size distributions and the complex refractive indices associated with each MOSAIC chemical constituent⁶⁷. This step requires assumptions on mixing state and morphology, for which WRF-Chem provides various options. For mixing state, we used the internal mixing option where the species were internally mixed within each MOSAIC size bin, which is the most realistic assumption based on atmospheric measurements¹¹⁰. We also used the spherical

core-shell morphology option, with BC residing in the core and the other components forming a well-mixed shell^{75,111,112}, in order to apply the core-shell Mie theory optical model¹¹³. We did not account for light-absorbing organic aerosols (brown carbon, BrC) in these simulations. A summary of other models and configurations used in the simulations is given in Table B1 in appendix B.

4.2.2. Experimental Design

We performed numerical experiments to estimate the public-health and direct radiative effects associated with the change in carbonaceous aerosol (BC and OA) concentrations due to shifting the U.S. gasoline vehicle fleet from PFI to GDI. To establish a baseline for these estimates, we also quantified the effects of the aerosol emissions from the gasoline fleet prior to shifting to GDI. We conducted three parallel WRF-Chem experiments with different aerosol emission factors from gasoline vehicles. In the first experiment, we set the gasoline-vehicle aerosol emissions to zero. This experiment, referred to as “no-gasoline,” served as a control for the other two experiments. The gasoline-vehicle aerosol emissions in the second experiment were obtained from the NEI-2011 emission inventory⁸⁵. Since the NEI-2011 emission inventory was based on laboratory measurements of PFI vehicles¹¹⁴, the difference between this experiment, referred to as “PFI,” and the “no-gasoline” experiment represents the baseline effect of gasoline vehicles prior to shifting to GDI. In the third experiment, referred to as “GDI,” we modified the NEI-2011 gasoline-vehicle aerosol emission factors assuming that the entire U.S. fleet was shifted from PFI to GDI. Therefore, the difference between the “GDI” and “PFI” experiments is not meant to capture the gradual shift from PFI to GDI technologies, but rather represents an upper-bound estimate that anticipates the endpoint of the rapid

proliferation of GDI vehicles^{46,47}. The effect of shifting from PFI to GDI, i.e. the difference between the “GDI” and “PFI” experiments, is represented as PFI → GDI.

We calculated the gasoline-vehicle aerosol emission factors in the “GDI” experiment based on the laboratory study of Saliba et al.⁵¹, which reported tailpipe emission factors of various gaseous and aerosol species from a comprehensive test fleet. In our calculations, we used the data from the study’s ULEV and SULEV vehicles, 20 of which had PFI engines (17 ULEV and 3 SULEV) and 13 had GDI engines (5 ULEV and 8 SULEV). We modified the NEI-2011 emission factors of BC and OC in the “GDI” experiment as:

$$EF_{\text{GDI}} = S \times EF_{\text{NEI-2011}} \quad (4.1)$$

Where EF_{GDI} and $EF_{\text{NEI-2011}}$ are the emission factors in the “GDI” experiment and NEI-2011 inventory, respectively, and $S = EF_{\text{GDI}} / EF_{\text{PFI}}$ is a scaling factor (4.22 for BC and 0.92 for OC) calculated as the ratio of the median GDI and PFI emissions reported in Saliba et al.⁵¹. Modifying the emission factors in this fashion captures the impacts of changes in engine technology while ensuring consistent miles driven across the simulations.

It is important to note that vehicle-to-vehicle variability as well as differences in measurement techniques and conditions lead to a large variability in reported aerosol emission factors, even for vehicles with the same engine technology and emission standards^{51,53,115}. Therefore, the emission factors from a single study are unlikely to capture the average behavior of the U.S. fleet represented in the NEI inventory. The advantage of our scaling approach is that it does not require the PFI emission measurements in Saliba et al.⁵¹ to be consistent with the NEI inventory, but rather that the scaling factor in equation (4.1) applies universally. This is justified because the PFI and

GDI emissions in Saliba et al.⁵¹ were measured from a comprehensive test fleet (20 PFI and 13 GDI) using the same instruments and under the same conditions, thus eliminating measurement inconsistencies. Furthermore, the BC scaling factor (4.22) we calculated from Saliba et al.⁵¹ is consistent with BC scaling factor (approximately 4.5) we calculated from the data reported in Zimmerman et al.¹⁰⁷. That study compiled a comprehensive set of BC emission factors from various studies that measured BC emissions from PFI and/or GDI vehicles. The agreement between the BC scaling factors calculated from the Saliba et al. and Zimmerman et al. data provides further confidence in our choice of BC scaling factor.

We executed the numerical experiments for 2 one-month simulation periods for the months of January and July of the year 2011 to capture seasonal variability. Each simulation started from identical initial conditions, with the first 10 days excluded from the analysis as spin-up time. Imposing consistent lateral boundary conditions and nudging the wind fields within the domain constrained difference in internal variability between the simulations, such that the differences in aerosol concentrations could be mostly attributed to emissions.

4.3. Results and Discussion

4.3.1. Model Validation

To validate the model output, we compared the monthly average BC, OA, and PM_{2.5} surface concentrations from the “PFI” experiments (i.e. using standard NEI-2011 emissions) with observations obtained from the Chemical Speciation Network (CSN)¹¹⁶ and the Interagency Monitoring of Protected Visual Environments (IMPROVE)¹¹⁶ network (Figure 4.1). CSN consists of 51 stations around the U.S., mostly in urban areas, and

IMPROVE consists of 110 stations that measure mostly background concentrations. Following Boylan and Russell¹ and Tessum et al.¹¹⁷, we assessed the model performance using three performance metrics: normalized mean error (NME), mean fractional error (MFE), and root-mean-square error (RMSE) (see appendix B). As shown in appendix B Figure B1, the model achieves the performance goals (defined by Boylan and Russell¹ as the performance the model should strive to achieve) for BC and OA for both the January and July simulations. For PM_{2.5}, the model achieves the performance criteria (defined by Boylan and Russell¹ as the performance necessary for regulatory purposes) for all model-observation comparisons except for the July IMPROVE comparison. We note that the error in the modeled PM_{2.5} in July is partly due to the high dust levels in the summer¹¹⁸, which are not captured well by the model. However, since this study focuses on the effects of aerosol emissions from vehicles (BC and OA), the error in PM_{2.5} concentrations associated with underestimating dust concentrations has minimal effect on the analysis presented in the subsequent sections.

We also used the same performance metrics (NME, MFE, and RMSE) to assess the model performance in predicting meteorological parameters (surface temperatures, incoming solar radiation fluxes, and horizontal wind speed) compared to observations from the Clean Air Status and Trends Network (CASTNET)¹¹⁹ measurements (Figure B2). Numerical values of the performance metrics for all meteorological parameters and particulate pollutants are given in appendix B Table B2.

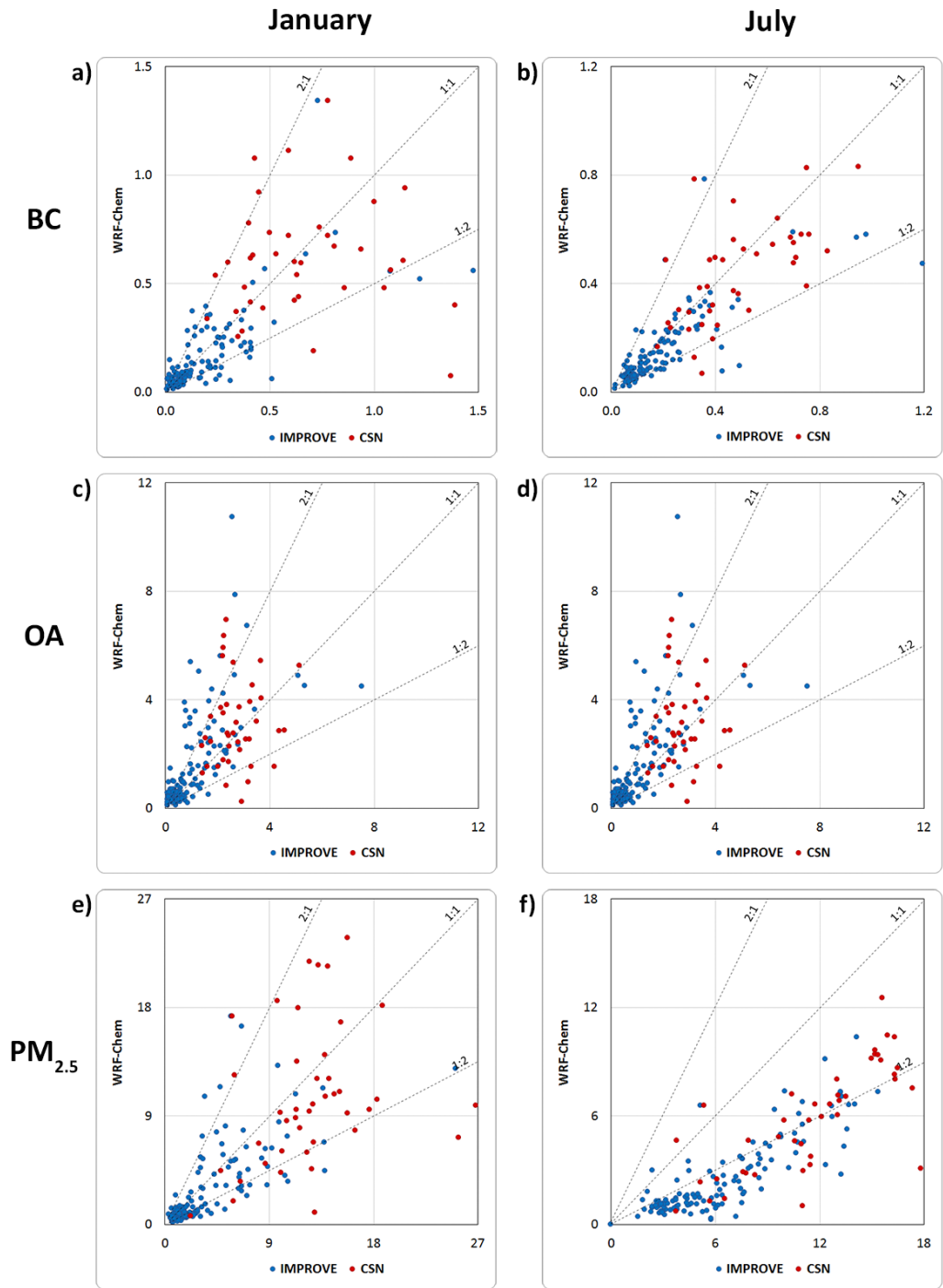


Figure 4.1. Comparison between monthly average BC, OA, and PM_{2.5} surface concentrations ($\mu\text{g}/\text{m}^3$) predicted by the model and obtained from IMPROVE (blue) and CSN (red) observational data for 2011. (a) BC, January. (b) BC, July. (c) OA, January. (d) OA, July. (e) PM_{2.5}, January. (f) PM_{2.5}, July.

4.3.2. The effect of Shifting from PFI to GDI on Aerosol Concentrations

We estimated the monthly (January and July) average BC, OA, and PM_{2.5} surface concentrations attributed to the 2011 U.S. gasoline (PFI) fleet emissions as the difference between surface concentrations in the “PFI” and “no-gasoline” experiments. Similarly, we estimated the BC, OA, and PM_{2.5} surface concentrations attributed to gasoline vehicles after shifting to GDI as the difference between surface concentrations in the “GDI” and “no-gasoline” experiments. Finally, we obtained the effect of shifting from PFI to GDI on the surface concentrations as the difference between surface concentrations in the “GDI” and “PFI” experiments. The results are shown in Figure 4.2 (BC), Figure 4.3 (OA), and Figure 4.4 (PM_{2.5}).

Comparing Figure 4.2b and 2f reveals that the contribution of gasoline vehicles to BC surface concentrations is stronger in January than in July. This is in part due to the fact that aerosol (BC and OA) emission factors from transportation sources exhibit an inverse relation with temperature¹¹⁴, leading to higher emissions in the winter. As expected, shifting from PFI to GDI results in a substantial increase in BC surface concentrations in both January (Figure 4.2c and 4.2d) and July (Figure 4.2g and 4.2h) due to the factor of 4.22 increase in BC emission factors (section 4.2.2).

Similar to BC, the OA surface concentrations attributed to gasoline vehicles in January are larger than in July (Figure 4.3b and 4.3f). And as expected, shifting from PFI to GDI results in a small decrease in OA surface concentrations in January (Figure 4.3c and 4.3d) due to the factor of 0.92 decrease in OA emission factors (section 2.2). Interestingly, the contribution of gasoline vehicles to OA surface concentrations in July is predicted to be negative in certain regions (Figure 4.3f and 4.3g). This is associated with the high levels

of biogenic emissions and consequently SOA formation in the summer, especially over the Eastern U.S.¹²⁰. Specifically, due to the feedback between radiative transfer, meteorology, and chemistry in WRF-Chem, aerosols affect the downward solar radiation and surface temperatures, which in turn affect the biogenic emission factors. Therefore, the differences in vehicle aerosol emissions between the “no-gasoline,” “PFI,” and “GDI” experiments induce differences in the biogenic emissions in the three experiments, leading to differences in SOA formation, and consequently OA surface concentrations (see Figure B3).

As shown in Figure 4.4, the change in January PM_{2.5} surface concentrations due to shifting from PFI to GDI is dominated by the relatively large increase in BC surface concentrations. On the other hand, the change in July PM_{2.5} surface concentrations due to shifting from PFI to GDI is less substantial. It is positive over regions where the increase in BC is dominant, and negative over some regions with high SOA concentrations, which are most sensitive to the decrease in biogenic emissions, as described in the previous paragraph.

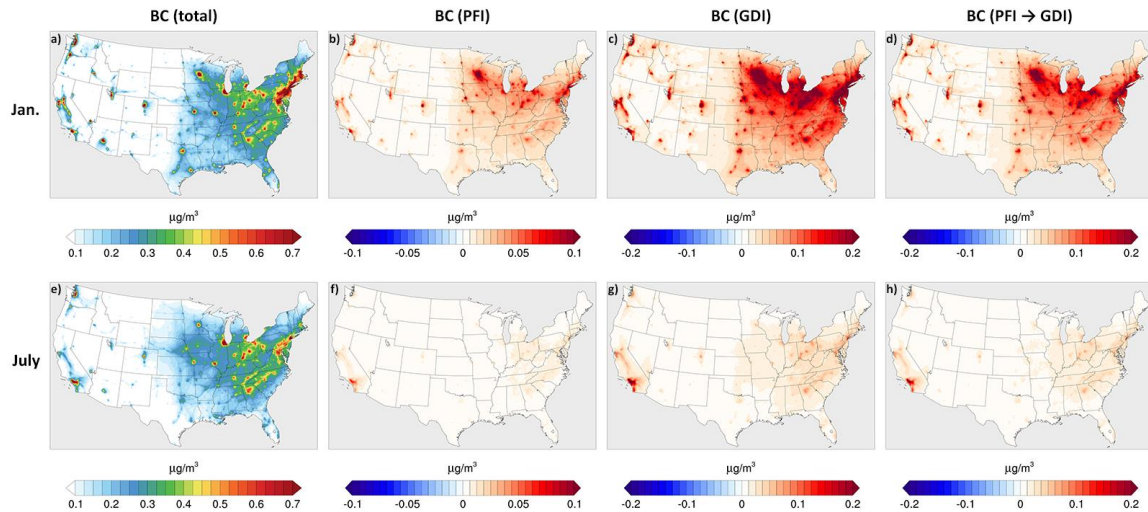


Figure 4.2. Monthly average BC surface concentrations in January (top panels) and July (bottom panels) 2011. Panels (a) and (e), obtained from the “PFI” experiments, correspond to the total BC concentrations. Panels (b) and (f), obtained as the difference between the “PFI” and “no-gasoline” experiments, correspond to the contribution of the 2011 gasoline fleet (PFI) to BC. Panels (c) and (g), obtained as the difference between the “GDI” and “no-gasoline” experiments, correspond to the contribution of gasoline vehicles to BC after shifting to GDI. Panels (d) and (h), obtained as the difference between the “GDI” and “PFI” experiments, correspond to the effect of shifting from PFI to GDI on BC.

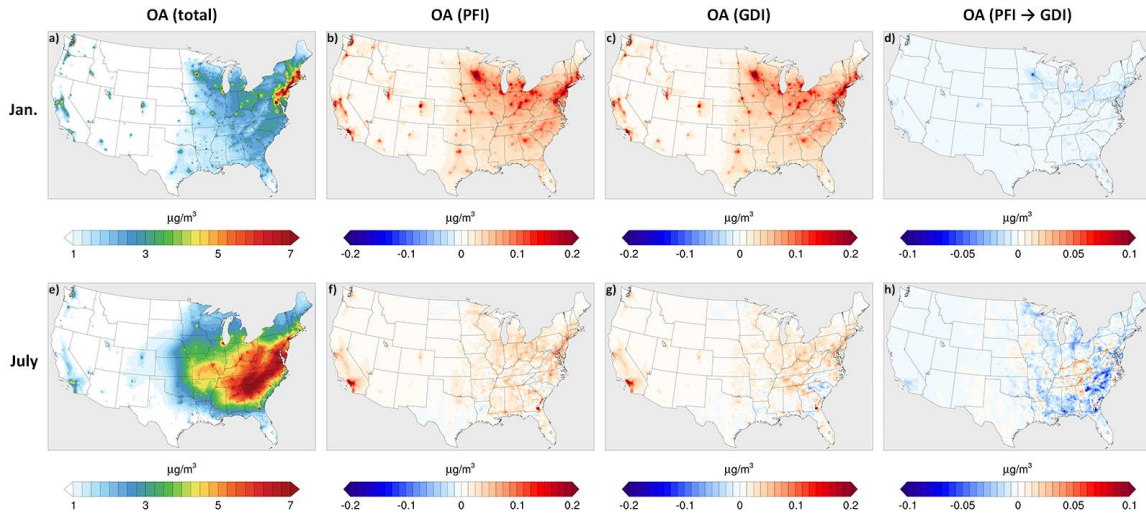


Figure 4.3. Monthly average OA surface concentrations in January (top panels) and July (bottom panels) 2011. Panels (a) and (e), obtained from the “PFI” experiments, correspond to the total OA concentrations. Panels (b) and (f), obtained as the difference between the “PFI” and “no-gasoline” experiments, correspond to the contribution of the 2011 gasoline fleet (PFI) to OA. Panels (c) and (g), obtained as the difference between the “GDI” and “no-gasoline” experiments, correspond to the contribution of gasoline vehicles to OA after shifting to GDI. Panels (d) and (h), obtained as the difference between the “GDI” and “PFI” experiments, correspond to the effect of shifting from PFI to GDI on OA.

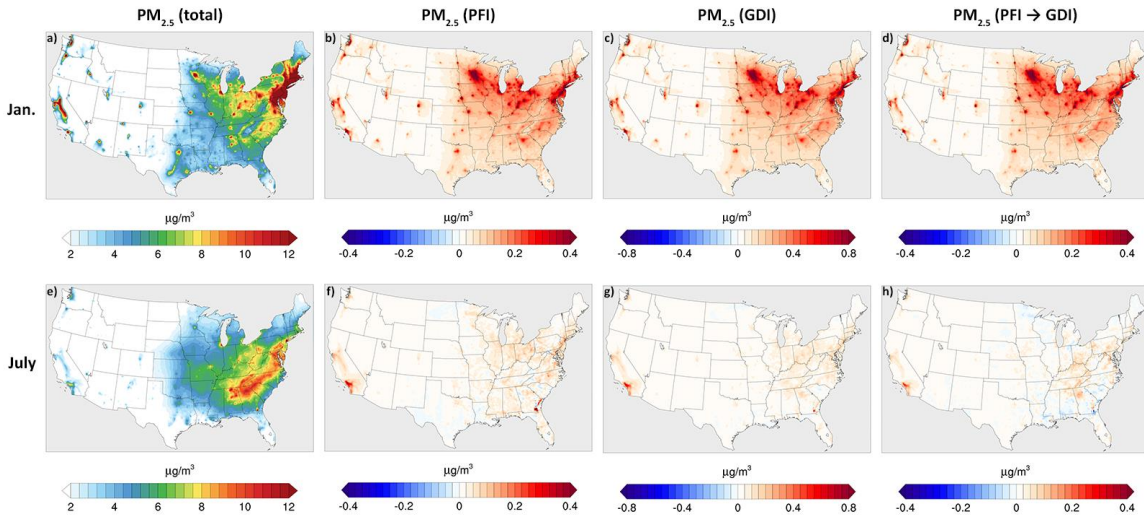


Figure 4.4. Monthly average $PM_{2.5}$ surface concentrations in January (top panels) and July (bottom panels) 2011. Panels (a) and (e), obtained from the “PFI” experiments, correspond to the total $PM_{2.5}$ concentrations. Panels (b) and (f), obtained as the difference between the “PFI” and “no-gasoline” experiments, correspond to the contribution of the 2011 gasoline fleet (PFI) to $PM_{2.5}$. Panels (c) and (g), obtained as the difference between the “GDI” and “no-gasoline” experiments, correspond to the contribution of gasoline vehicles to $PM_{2.5}$ after shifting to GDI. Panels (d) and (h), obtained as the difference between the “GDI” and “PFI” experiments, correspond to the effect of shifting from PFI to GDI on $PM_{2.5}$.

4.3.3. Public-Health Impacts of Shifting from PFI to GDI

We quantified the public-health impacts of the increase in $PM_{2.5}$ concentrations associated with shifting from PFI to GDI in terms of the increase in $PM_{2.5}$ -related mortality rates compared to the baseline $PM_{2.5}$ -related mortality rates attributed to gasoline vehicles. Due to the absence of reliable epidemiological data on species-specific health effects^{61,121}, these calculations followed the EPA methodology of assigning the

same health effects to all PM_{2.5} species¹²². We calculated spatially resolved attributable fractions (AF), defined as the ratio of PM_{2.5}-related mortality to total all-cause mortality¹²³:

$$AF=1-\exp(-\beta C) \quad (4.2)$$

The derivation of equation (4.2) is given in the appendix B. β (m³/μg) is the concentration-response factor, calculated from epidemiological data as 0.005827¹²⁴ and C is the modeled yearly average – assumed to be the average of January and July experiments – PM_{2.5} surface concentrations (μg/m³) attributed to gasoline vehicle emissions. To validate the assumption that the average of January and July PM_{2.5} concentrations are representative of the annual averages, we investigated the applicability of this assumption to CSN/IMPROVE observations. We compared the annual average PM_{2.5} concentrations to the January/July averages from observations at each CSN/IMPROVE location. As shown in Figure B4, the median, 25th percentile, and 75% percentile of the relative differences for CSN and IMPROVE are 27.3%, 1.4%, and 36.2%, respectively and -1.3%, -13.3%, and 20.5%, respectively. Since our analysis focuses on the public-health impacts of vehicle PM_{2.5} emissions, which are mostly carbonaceous (BC and OA), we also performed similar comparison but for the BC + OA fraction of PM_{2.5}. Figure B5 shows the relative difference in BC + OA concentrations between annual and January/July averages at each CSN/IMPROVE location. The median, 25th percentile, and 75% percentile of the relative differences for CSN are 11.1%, -2.9%, and 21.7%, respectively and for IMPROVE are 3.9%, -13.0%, and 18.8%, respectively, thus supporting our use of January/July averages to represent annual averages.

Figure 4.5a shows yearly county-averaged AF associated with annual baseline gasoline-vehicle emissions in 2011. As expected, the fraction of premature mortality attributed to

gasoline-vehicle PM_{2.5} emissions is greatest in counties with high population / vehicle densities. As shown in Figure 4.5b and 4.5c, shifting the U.S. gasoline fleet from PFI to GDI is predicted to almost double the number of premature deaths attributed to gasoline-vehicle PM_{2.5}. Using county-resolved annual premature mortality (Y) data from the Center for Disease Control and Prevention (CDC) (<http://wonder.cdc.gov/ucd-icd10.html>, accessed on 06/07/2019), we calculated the total premature deaths associated with PM_{2.5} emitted by gasoline vehicles in the U.S. as:

$$M = \sum (AF \times Y) \tag{4.3}$$

Our calculations suggest that in 2011, 855 premature deaths were associated with PM_{2.5} vehicle emissions. This is in good agreement with the findings of Turner et al. (2015)⁶, who estimated that in 2008, 600 premature deaths were attributed to gasoline-emitted BC. Our calculations indicate that shifting to GDI results in a total 1599 premature deaths attributed to gasoline-emitted PM_{2.5}, an increase of 744 deaths over PFI.

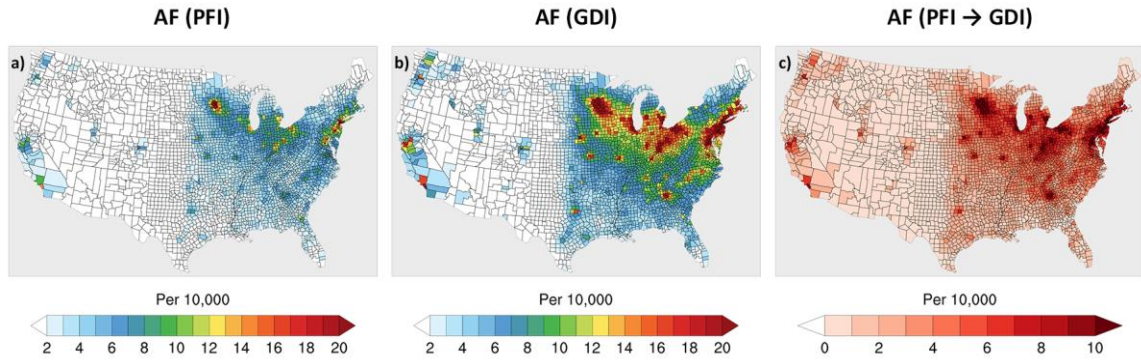


Figure 4.5. Annual average attributable fraction (AF) associated with $PM_{2.5}$ emitted by gasoline vehicles. The color scale represents the number of $PM_{2.5}$ -induced deaths per 10,000 all-cause premature deaths. (a) AF associated with baseline gasoline emissions in 2011 (PFI), calculated based on $PM_{2.5}$ concentrations obtained as the difference between the “PFI” and “no-gasoline” experiments. (b) AF associated with gasoline emissions after shifting to GDI, calculated based on $PM_{2.5}$ concentrations obtained as the difference between the “GDI” and “no-gasoline” experiments. (c) The effect of shifting from PFI to GDI on AF, calculated as the difference between (b) and (a).

Using the EPA recommended mean value of statistical life (VSL) of \$8 million¹²⁵, the annual social cost of premature deaths attributed to gasoline-vehicle $PM_{2.5}$ emissions is estimated at \$6.84 billion in 2011. Shifting from PFI to GDI would increase the annual social cost by \$5.95 billion to a total of \$12.79 billion. While these calculations involve assumptions on several levels (a complete shift from PFI to GDI, uniformity of the $PM_{2.5}$ concentration-response function, in addition to assumptions embedded in any attempt to monetize a social cost), they indicate that the public-health impacts of shifting the U.S. gasoline fleet to GDI technology imposes a non-negligible social cost. This cost should be weighed against the social benefits associated with the enhanced fuel economy and reduction in CO_2 emissions. Furthermore, it is important to note that our calculations

represent $12 \text{ km} \times 12 \text{ km}$ grid averages and do not capture the acute exposure to high levels of $\text{PM}_{2.5}$ that affects communities in close proximity to major roadways^{126,127}. An increase in vehicle $\text{PM}_{2.5}$ emissions disproportionately affects these, usually vulnerable¹²⁶, communities.

4.3.4. Direct Radiative Effect of Shifting from PFI to GDI

We calculated the monthly average (January and July 2011) direct radiative effect (DRE) of carbonaceous aerosols emitted by gasoline vehicles as:

$$\text{DRE} = \uparrow f_0 - \uparrow f_{\text{aerosol}} \quad (4.4)$$

Where $\uparrow f_0$ is the net upward shortwave flux at the top of the atmosphere without gasoline-emitted carbonaceous aerosols, obtained from the “no-gasoline” experiment, and $\uparrow f_{\text{aerosol}}$ is the upward flux with the gasoline-emitted carbonaceous aerosols, obtained from either the “PFI” or “GDI” experiments. We note that the DRE defined in equation (4.4) is not species-specific as is often the case in aerosol DRE calculations (e.g. DRE of BC), but is source-specific as it corresponds to the DRE of carbonaceous aerosols (BC and OA) emitted by gasoline vehicles. To stress this distinction, we use the notation DRE_{PFI} and DRE_{GDI} . We also define the DRE associated with shifting from PFI to GDI as:

$$\text{DRE}_{\text{PFI} \rightarrow \text{GDI}} = \text{DRE}_{\text{GDI}} - \text{DRE}_{\text{PFI}} \quad (4.5)$$

Figure 4.6 shows the monthly average (January and July 2011) DRE_{PFI} , DRE_{GDI} , and $\text{DRE}_{\text{PFI} \rightarrow \text{GDI}}$. Due to the feedback between radiation, chemical-transport, and meteorology in WRF-Chem, the difference in emissions, and consequently radiative balance, between the “no-gasoline,” “PFI,” and “GDI” experiments resulted in slight differences in meteorological conditions and SOA formation rates. This was manifested as noise in DRE over the highly resolved $12 \text{ km} \times 12 \text{ km}$ WRF-Chem grid. The DRE values in Figure 4.6

represent spatial averages over U.S. climate divisions¹²⁸. Due to the competing warming effect of BC and cooling effect of OA, the January DRE_{PFI} values range from slightly negative to slightly positive, with the exception of some Midwestern and Northeastern regions (Figure 4.6a). The magnitude of the July DRE_{PFI} values (Figure 4.6d) are smaller than January, which is in-line with the lower BC concentrations attributed to gasoline-vehicle emissions in July (see Figure 4.2), but could also be partly associated with differences in geophysical factors that affect the atmospheric radiative balance. Overall, the carbonaceous aerosol emissions by the (PFI) 2011 gasoline fleet exhibit an almost neutral direct radiative effect over the U.S., with spatially averaged DRE_{PFI} values of +0.031 and +0.015 W/m^2 in January and July, respectively. The significant increase in BC emissions associated with shifting to GDI results in a positive DRE_{GDI} and $DRE_{PFI \rightarrow GDI}$, as shown in Figure 4.6b, 4.6c, 4.6e, and 4.6f. As expected, the direct radiative effect is most prominent over regions with high vehicle densities in the Eastern U.S. and to a lesser extent over California. Furthermore, in the Northeastern U.S., the direct radiative effect in January ($DRE_{GDI \rightarrow PFI}$ up to +0.84 W/m^2) is significantly stronger than in July ($DRE_{GDI \rightarrow PFI}$ up to +0.18 W/m^2). As discussed above, this could be in part attributed to the fact that the aerosol emission factors of gasoline vehicles increase with decreasing temperature¹¹⁴. Therefore, the increase in BC emissions is more significant during the winter, leading to larger $DRE_{PFI \rightarrow GDI}$ values. This effect is most prominent in the Northeastern U.S. as it experiences the coldest winters among the U.S. regions. Another contributor to the large January $DRE_{PFI \rightarrow GDI}$ over the Northeastern U.S. is the high surface albedo due to snow accumulation in the winter (see Figure B6).

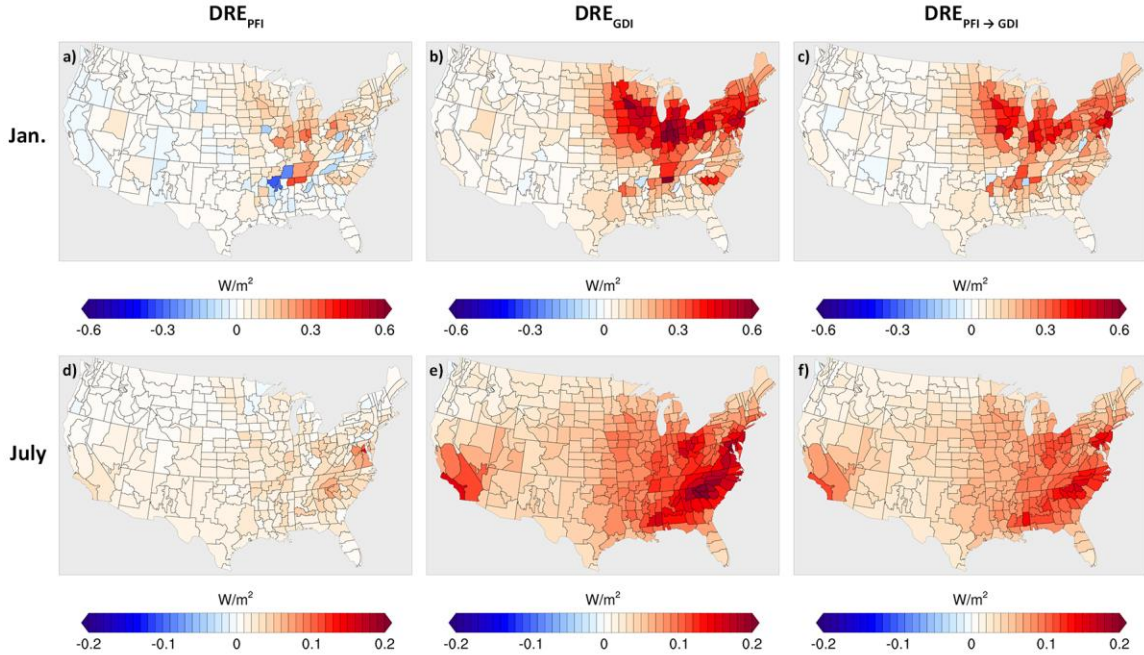


Figure 4.6. Monthly average direct radiative effect (DRE) of carbonaceous aerosols emitted by gasoline vehicles for January (top panels) and July (bottom panels) 2011. The left panels (a and d) correspond to DRE_{PFI} , the DRE associated with the 2011 gasoline fleet (PFI), obtained as the difference in radiative balance between the “PFI” and “no-gasoline” simulations. The middle panels (b and e) correspond to DRE_{GDI} , the DRE associated with the gasoline vehicles after shifting to GDI, obtained as the difference in radiative balance between the “PFI” and “no-gasoline” simulations. The right panels (c and f) correspond to $DRE_{PFI \rightarrow GDI}$, the DRE associated with shifting from PFI to GDI, calculated as the difference between the middle and left panels (equation 4.5).

4.3.5. Climate Trade-off of Shifting from PFI to GDI

When discussing the climate implications of shifting the U.S. gasoline fleet from PFI to GDI technology, it is important to present the discussion within the context of relevant spatial and temporal scales. For instance, the mean $DRE_{PFI \rightarrow GDI}$ over the whole U.S. is modest ($+0.10 \text{ W/m}^2$ for January and $+0.05 \text{ W/m}^2$ for July), and the global-mean

$DRE_{PFI \rightarrow GDI}$ is expected to be even smaller. However, due to the short atmospheric lifetime of aerosols (days⁶⁴), the local $DRE_{PFI \rightarrow GDI}$ exhibits large values over source regions, as evident in Figure 4.6. On the other hand, the atmospheric lifetime of CO_2 is up to 200 years¹²⁹, resulting in a large-capacitance system that exhibits well-mixed behavior and, consequently, a globally uniform CO_2 radiative effect¹³⁰. Therefore, even over regions with high vehicle emissions (e.g. the Northeastern U.S.), the local radiative effect associated with the reduction in CO_2 due to shifting from PFI to GDI ($RE_{CO_2, PFI \rightarrow GDI}$) is similar in magnitude to the global-mean $RE_{CO_2, PFI \rightarrow GDI}$, which is expected to be relatively small (see below). On the other hand, $DRE_{PFI \rightarrow GDI}$ over these source regions is much larger in magnitude than the global-mean $DRE_{PFI \rightarrow GDI}$, and is expected to be much stronger than $RE_{CO_2, PFI \rightarrow GDI}$. Furthermore, the atmospheric concentrations of BC, thus its direct radiative effect, relaxes to a new steady state on a timescale of days in response to a change in emission profiles. Therefore, the BC-induced climate burden (warming) due to shifting from PFI to GDI is realized over much shorter timescales than the climate benefit (cooling) of the reduction in CO_2 .

We compared $DRE_{PFI \rightarrow GDI}$ calculated in section 3.4 to first-order estimates of $RE_{CO_2, PFI \rightarrow GDI}$ assuming globally well-mixed CO_2 and therefore, globally uniform $RE_{CO_2, PFI \rightarrow GDI}$ (see appendix B for calculation details). Therefore, the $RE_{CO_2, PFI \rightarrow GDI}$ obtained from this calculation is assumed to be equal to the local $RE_{CO_2, PFI \rightarrow GDI}$ over a certain region and can be compared with the $DRE_{PFI \rightarrow GDI}$ over the same region to obtain the net local radiative effect associated with the trade-off between the increase in BC emissions and decrease in CO_2 emissions. To estimate the decrease in CO_2 concentrations, we considered an extreme upper-bound scenario corresponding to 1) a complete shift of the global gasoline fleet from

PFI to GDI and 2) a 15% reduction in gasoline-vehicle CO₂ emissions due to the shift, which is the high end of the estimates in Zimmerman et al.⁶³. We then calculated the yearly average RE_{CO₂,PFI→GDI} after the shift (Figure B7). Even with these extreme estimates in CO₂ reduction, RE_{CO₂,PFI→GDI} is only -0.013 W/m² after 20 years. The reason is that gasoline vehicles contribute approximately 7% of the global CO₂ emissions¹³¹, and therefore, a global shift from PFI to GDI corresponds to only 1% reduction in global CO₂ emissions. The yearly average DRE_{PFI→GDI} over the U.S., taken as the average of the January and July experiments in section 3.3, is +0.075 W/m², more than a factor of 5 larger than RE_{CO₂,PFI→GDI}. The difference is even larger over climate divisions with high vehicle densities in the Northeast and the Midwest (Figure 4.5), where the yearly average DRE_{PFI→GDI} is as high as +0.45 W/m².

The seeming inconsistency between our findings and those of previous studies that reported net climate benefits (i.e. negative net radiative effect) of shifting from PFI to GDI using the global warming potential (GWP) framework^{51,63} is due to the difference in spatial scales considered in the analyses. The GWP framework provides a simplified global-mean comparison of the energy absorbed by a pollutant (in this case BC) versus CO₂ over a certain time horizon, and therefore does not provide information on the local/regional trade-off of shifting from PFI to GDI. On the other hand, our analysis utilizes a regional modeling framework that resolves these localized effects. Furthermore, the GWP analysis only provides information on whether the net effect is negative or positive^{51,63}, but does not provide quantitative estimates of the magnitude of the net radiative effect (i.e. in W/m²). As described above, a high-end estimate of RE_{CO₂,PFI→GDI} is only -0.013 W/m² over a 20-year time horizon. Therefore, even if we ignore the global-mean DRE_{PFI→GDI}, the net

global-mean radiative effect of shifting from PFI to GDI and the associated climate benefits (e.g. the effect on global-mean temperatures) are expected to be minimal.

4.3.6. Implications

The calculations and discussion in section 3.4 and 3.5 illustrate the importance of the spatial scales considered for quantifying the climate trade-off associated with the emerging GDI technology due to the difference in spatial scales at which BC (aerosols) and CO₂ (well-mixed green-house gases) exert their influence¹⁰⁸. A shift from PFI to GDI is expected to yield net global-mean climate benefits (e.g. a decrease in global-mean temperature). However, the magnitude of this effect (i.e. in W/m²) is expected to be rather small because gasoline vehicles contribute only 7% of the global CO₂ emissions¹³¹. Therefore, the reduction in gasoline-vehicle CO₂ emissions due to shifting from PFI to GDI has a minimal effect on atmospheric CO₂ concentrations. On the other hand, the increase in BC emissions imposes localized acute impacts both on public health (Figure 4.5) and direct radiative effect (Figure 4.6). While a quantitative economic analysis that weighs the social costs associated with these impacts against the benefits associated with the reduction in CO₂ emissions¹³² is beyond the scope of this work, our results provide strong evidence that such analysis is necessary for developing robust policy vis-à-vis the position of GDI in the landscape of future vehicle technologies. We note that the results obtained in this study do not account for the potential of incorporating gasoline particulate filters (GPFs) for reducing BC emissions from GDI vehicles. GPFs impose a penalty on fuel economy and are subject to technical challenges that need to be resolved before reliable practical implementation¹⁰⁷. Our results suggest that the development and

implementation of GPFs is crucial for GDI engines to be a viable solution for enhanced fuel economy without compromising air quality.

Funding Sources

Financial support was provided by the National Science Foundation, Division of Atmospheric and Geospace Sciences (AGS-1748080), the U.S. Department of Energy Regional and Global Model Analysis program (DE-SC0019459), and the University of Georgia President Interdisciplinary Seed Grant Initiative.

CHAPTER 5

CONCLUSIONS, FUTURE WORK, AND LIMITATIONS

We used WRF-Chem as a regional climate model and observational datasets to improve the representation of CA's concentrations, optical properties, radiative effects, and public health effects in the U.S.. More specifically, the two main objectives of this dissertation are to: (1) account for the light absorption of BrC emitted from biomass burning (wildfires) in WRF-Chem model and quantify its effect on aerosol optical properties, and (2) estimate the public health and direct radiative effect of the change in CA emissions associated with shifting the U.S. gasoline light-duty vehicles fleet from PFI to GDI engines.

For the first objective, we employed a comprehensive set of optical properties retrieved from AERONET observations as complementary constraints for testing the representation of wildfire BrC in WRF-Chem. Specifically, the combination of AAOD (an extensive aerosol light-absorption property) and AAE (a pseudo-intensive light-absorption property that describes the wavelength dependence of absorption) comparisons showed that BrC absorption should be accounted for in order to reconcile model and observed absorption. One could match model and observed AAOD at a certain wavelength by scaling wildfire BC emissions, but that would lead to disagreement at other wavelengths if BrC absorption was ignored. Overall, the best model-observation agreement in terms of aerosol absorption was achieved by representing wildfire BrC absorption using the parameterization of Saleh et al.¹¹ and its decay by photobleaching

using the parameterization of Wang et al.⁴³. However, in order to also reconcile model and observed AOD and SSA, we found that the model should account for relatively high levels of wildfire SOA (similar levels to wildfire POA). Neglecting wildfire SOA results in severely underestimating aerosol scattering. This finding indicates that modeling frameworks that do not account for wildfire SOA underestimate exposure to aerosols in regions impacted by wildfire emissions. For future work, the simulations can be improved in several ways. In this study, for simplicity, we used a zeroth-order approximation in the model to represent SOA formation from wildfire emissions, where SOA was emitted directly with POA. The SOA formation can be parameterized in the model to reflect time-dependent conversion of VOCs to SOA that depend on atmospheric age and oxidant (e.g. OH) concentrations. Furthermore, one limitation in implementing BrC light absorption parameterization in the model is that wildfire BC-to-OA ratio in the emission inventory used in this study is only based on the fuel (land-cover) type^{32,133}. However, wildfire BC-to-OA ratio also depends on combustion conditions^{11,23}. There are no modeling frameworks that account for this dependence, but future work in our group aims to exploit satellite observations to categorize wildfires based on their intensities and utilize this information to represent the dependence of BC-to-OA ratio on combustion conditions. Finally, the simulations in this study focused only on the month of August 2015, which was used as a natural experiment to constraint the effect of BrC in wildfire emissions. In order to assess the effect of wildfire emissions on radiative transfer and air quality, future work will involve running the model for an extended simulation period (e.g. one year) instead of one-month period, which provides enough results to estimate

annual radiative effect of BrC light absorption as well as the surface concentrations of wildfire CA and their health effects.

For the second objective, we modified BC and OA emissions from gasoline light-duty vehicles in the emission inventory based on measurement studies to investigate the public-health and direct radiative effect of shifting from PFI to GDI engines. The results show that the premature deaths associated with BC and OA (i.e. $PM_{2.5}$) vehicle emissions and, therefore, the social cost, would be doubled after shifting the gasoline vehicles fleet to GDI technology. It is important to note that the public health cost of shifting to GDI engines varies significantly over the U.S., with very strong public health effect in urban regions with high vehicle density and negligible effect over less populated regions. The (relatively fine) 12 km grid resolution used in this study captures the contrast between urban and rural areas. However, we expect that there are large variations in $PM_{2.5}$ levels near major roadways that occur at sub-km length scales and thus are not captured in our simulations. The high levels of $PM_{2.5}$ mostly impact near-roadway, usually low-income, communities. The simulated DRE also shows that switching gasoline vehicles from PFI to GDI engines leads to a warming effect over the U.S., especially during cold months of the year and over regions with high vehicle density. On the other hand, this shift has a global evenly distributed climate benefit (cooling effect) due to the decrease in CO_2 emissions from GDI engines. Our study suggests that, at regional scale, the warming effect associated with increase in BC emission from GDI engines is stronger than the cooling effect due to reduction in CO_2 . It is important to note that in this study we assumed a complete instantaneous switch of the U.S. gasoline light-duty vehicles fleet

from PFI to GDI engines. In future works, we can construct different scenarios that involve a more realistic gradual shift from PFI to GDI.

REFERENCES

- (1) Boylan, J. W.; Russell, A. G. PM and Light Extinction Model Performance Metrics, Goals, and Criteria for Three-Dimensional Air Quality Models. *Atmos. Environ.* **2006**, *40* (26), 4946–4959.
- (2) Hinds, W. C. *Aerosol Technology: Properties, Behavior, and Measurement of Airborne Particles, 2nd Edition*; Wiley, 1999.
- (3) Fann, N.; Lamson, A. D.; Anenberg, S. C.; Wesson, K.; Risley, D.; Hubbell, B. J. Estimating the National Public Health Burden Associated with Exposure to Ambient PM_{2.5} and Ozone. *Risk Anal.* **2012**, *32* (1), 81–95.
- (4) Haeffliger, O. P.; Bucheli, T. D.; Zenobi, R. Laser Mass Spectrometric Analysis of Organic Atmospheric Aerosols. 1. Characterization of Emission Sources. *Environ. Sci. Technol.* **2000**.
- (5) Janssen, N. A. H.; Hoek, G.; Simic-Lawson, M.; Fischer, P.; van Bree, L.; Brink, H. Ten; Keuken, M.; Atkinson, R. W.; Ross Anderson, H.; Brunekreef, B.; et al. Black Carbon as an Additional Indicator of the Adverse Health Effects of Airborne Particles Compared with Pm₁₀ and Pm_{2.5}. *Environmental Health Perspectives*. 2011.
- (6) Turner, M. D.; Henze, D. K.; Hakami, A.; Zhao, S.; Resler, J.; Carmichael, G. R.; Stanier, C. O.; Baek, J.; Sandu, A.; Russell, A. G.; et al. Differences between Magnitudes and Health Impacts of BC Emissions across the United States Using

- 12 Km Scale Seasonal Source Apportionment. *Environ. Sci. Technol.* **2015**, *49* (7), 4362–4371.
- (7) Chung, S. H.; Seinfeld, J. H. Global Distribution and Climate Forcing of Carbonaceous Aerosols. *J. Geophys. Res. Atmos.* **2002**.
- (8) Bond, T. C.; Doherty, S. J.; Fahey, D. W.; Forster, P. M.; Berntsen, T.; Deangelo, B. J.; Flanner, M. G.; Ghan, S.; Kärcher, B.; Koch, D.; et al. Bounding the Role of Black Carbon in the Climate System: A Scientific Assessment. *J. Geophys. Res. Atmos.* **2013**, *118* (11), 5380–5552.
- (9) Jacobson, M. Z. Strong Radiative Heating Due to the Mixing State of Black Carbon in Atmospheric Aerosols. *Nature* **2001**, *409* (6821), 695–697.
- (10) Kanakidou, M.; Seinfeld, J. H.; Pandis, S. N.; Barnes, I.; Dentener, F. J.; Facchini, M. C.; Van Dingenen, R.; Ervens, B.; Nenes, A.; Nielsen, C. J.; et al. Organic Aerosol and Global Climate Modelling: A Review. *Atmos. Chem. Phys.* **2005**.
- (11) Saleh, R.; Robinson, E. S.; Tkacik, D. S.; Ahern, A. T.; Liu, S.; Aiken, A. C.; Sullivan, R. C.; Presto, A. A.; Dubey, M. K.; Yokelson, R. J.; et al. Brownness of Organics in Aerosols from Biomass Burning Linked to Their Black Carbon Content. *Nat. Geosci.* **2014**, *7* (9), 647–650.
- (12) Jaffe, D. A.; O’Neill, S. M.; Larkin, N. K.; Holder, A. L.; Peterson, D. L.; Halofsky, J. E.; Rappold, A. G. Wildfire and Prescribed Burning Impacts on Air Quality in the United States. *Journal of the Air and Waste Management Association*. 2020.
- (13) Fann, N.; Alman, B.; Broome, R. A.; Morgan, G. G.; Johnston, F. H.; Pouliot, G.; Rappold, A. G. The Health Impacts and Economic Value of Wildland Fire

- Episodes in the U.S.: 2008–2012. *Sci. Total Environ.* **2018**, 610–611.
- (14) Larsen, A. E.; Reich, B. J.; Ruminiski, M.; Rappold, A. G. Impacts of Fire Smoke Plumes on Regional Air Quality, 2006-2013 Article. *Journal of Exposure Science and Environmental Epidemiology*. 2018.
- (15) Sokolik, I. N.; Soja, A. J.; DeMott, P. J.; Winker, D. Progress and Challenges in Quantifying Wildfire Smoke Emissions, Their Properties, Transport, and Atmospheric Impacts. *J. Geophys. Res. Atmos.* **2019**, 124 (23).
- (16) Core Writing Team; Pachauri, R. K.; Meyer, L. *Climate Change 2014: Synthesis Report. Contribution of Working Groups I, II and III to the Fifth Assessment Report of the Intergovernmental Panel on Climate Change*; Geneva, Switzerland, 2014.
- (17) O'Brien, J. J.; Hiers, J. K.; Varner, J. M.; Hoffman, C. M.; Dickinson, M. B.; Michaletz, S. T.; Loudermilk, E. L.; Butler, B. W. Advances in Mechanistic Approaches to Quantifying Biophysical Fire Effects. *Current Forestry Reports*. 2018.
- (18) Hiers, J. K.; O'Brien, J. J.; Varner, J. M.; Butler, B. W.; Dickinson, M.; Furman, J.; Gallagher, M.; Godwin, D.; Goodrick, S. L.; Hood, S. M.; et al. Prescribed Fire Science: The Case for a Refined Research Agenda. *Fire Ecol.* **2020**, 16 (1).
- (19) Brown, H.; Liu, X.; Pokhrel, R.; Murphy, S.; Lu, Z.; Saleh, R.; Mielonen, T.; Kokkola, H.; Bergman, T.; Myhre, G.; et al. Biomass Burning Aerosols in Most Climate Models Are Too Absorbing. *Nat. Commun.* **2021**, 12 (1).
- (20) Flannigan, M. D.; Krawchuk, M. A.; De Groot, W. J.; Wotton, B. M.; Gowman, L. M. Implications of Changing Climate for Global Wildland Fire. *International*

Journal of Wildland Fire. 2009.

- (21) U.S. Environmental Protection Agency (EPA). *Renewable Fuel Standard Program (RFS2) Regulatory Impact Analysis*; 2010.
- (22) Knorr, W.; Dentener, F.; Lamarque, J. F.; Jiang, L.; Arneth, A. Wildfire Air Pollution Hazard during the 21st Century. *Atmos. Chem. Phys.* **2017**, *17* (14).
- (23) McClure, C. D.; Lim, C. Y.; Hagan, D. H.; Kroll, J. H.; Cappa, C. D. Biomass-Burning-Derived Particles from a Wide Variety of Fuels - Part 1: Properties of Primary Particles. *Atmos. Chem. Phys.* **2020**, *20* (3).
- (24) Adler, G.; Wagner, N. L.; Lamb, K. D.; Manfred, K. M.; Schwarz, J. P.; Franchin, A.; Middlebrook, A. M.; Washenfelder, R. A.; Womack, C. C.; Yokelson, R. J.; et al. Evidence in Biomass Burning Smoke for a Light-Absorbing Aerosol with Properties Intermediate between Brown and Black Carbon. *Aerosol Sci. Technol.* **2019**, *53* (9).
- (25) Pokhrel, R. P.; Wagner, N. L.; Langridge, J. M.; Lack, D. A.; Jayarathne, T.; Stone, E. A.; Stockwell, C. E.; Yokelson, R. J.; Murphy, S. M. Parameterization of Single-Scattering Albedo (SSA) and Absorption Ångström Exponent (AAE) with EC/OC for Aerosol Emissions from Biomass Burning. *Atmos. Chem. Phys.* **2016**, *16* (15), 9549–9561.
- (26) Forrister, H.; Liu, J.; Scheuer, E.; Dibb, J.; Ziemba, L.; Thornhill, K. L.; Anderson, B.; Diskin, G.; Perring, A. E.; Schwarz, J. P.; et al. Evolution of Brown Carbon in Wildfire Plumes. *Geophys. Res. Lett.* **2015**, *42* (11).
- (27) Zhang, Y.; Forrister, H.; Liu, J.; Dibb, J.; Anderson, B.; Schwarz, J. P.; Perring, A. E.; Jimenez, J. L.; Campuzano-Jost, P.; Wang, Y.; et al. Top-of-Atmosphere

- Radiative Forcing Affected by Brown Carbon in the Upper Troposphere. *Nat. Geosci.* **2017**, *10* (7).
- (28) Liu, J.; Scheuer, E.; Dibb, J.; Diskin, G. S.; Ziemba, L. D.; Thornhill, K. L.; Anderson, B. E.; Wisthaler, A.; Mikoviny, T.; Devi, J. J.; et al. Brown Carbon Aerosol in the North American Continental Troposphere: Sources, Abundance, and Radiative Forcing. *Atmos. Chem. Phys.* **2015**, *15* (14).
- (29) Laskin, A.; Laskin, J.; Nizkorodov, S. A. Chemistry of Atmospheric Brown Carbon. *Chemical Reviews*. 2015.
- (30) Andreae, M. O.; Gelencsér, A. Black Carbon or Brown Carbon? The Nature of Light-Absorbing Carbonaceous Aerosols. *Atmos. Chem. Phys.* **2006**.
- (31) Saleh, R. From Measurements to Models: Toward Accurate Representation of Brown Carbon in Climate Calculations. *Current Pollution Reports*. 2020.
- (32) Akagi, S. K.; Yokelson, R. J.; Wiedinmyer, C.; Alvarado, M. J.; Reid, J. S.; Karl, T.; Crouse, J. D.; Wennberg, P. O. Emission Factors for Open and Domestic Biomass Burning for Use in Atmospheric Models. *Atmos. Chem. Phys.* **2011**, *11* (9).
- (33) Hammer, M. S.; Martin, R. V.; Van Donkelaar, A.; Buchard, V.; Torres, O.; Ridley, D. A.; Spurr, R. J. D. Interpreting the Ultraviolet Aerosol Index Observed with the OMI Satellite Instrument to Understand Absorption by Organic Aerosols: Implications for Atmospheric Oxidation and Direct Radiative Effects. *Atmos. Chem. Phys.* **2016**, *16* (4), 2507–2523.
- (34) Jo, D. S.; Park, R. J.; Lee, S.; Kim, S. W.; Zhang, X. A Global Simulation of Brown Carbon: Implications for Photochemistry and Direct Radiative Effect.

- Atmos. Chem. Phys.* **2016**, *16* (5).
- (35) Lin, G.; Penner, J. E.; Flanner, M. G.; Sillman, S.; Xu, L.; Zhou, C. Radiative Forcing of Organic Aerosol in the Atmosphere and on Snow: Effects of SOA and Brown Carbon. *J. Geophys. Res.* **2014**, *119* (12), 7453–7476.
- (36) Lu, Z.; Streets, D. G.; Winijkul, E.; Yan, F.; Chen, Y.; Bond, T. C.; Feng, Y.; Dubey, M. K.; Liu, S.; Pinto, J. P.; et al. Light Absorption Properties and Radiative Effects of Primary Organic Aerosol Emissions. *Environ. Sci. Technol.* **2015**, *49* (8), 4868–4877.
- (37) Saleh, R.; Cheng, Z.; Atwi, K. The Brown-Black Continuum of Light-Absorbing Combustion Aerosols. *Environ. Sci. Technol. Lett.* **2018**, *5* (8).
- (38) Wong, J. P. S.; Nenes, A.; Weber, R. J. Changes in Light Absorptivity of Molecular Weight Separated Brown Carbon Due to Photolytic Aging. *Environ. Sci. Technol.* **2017**, *51* (15).
- (39) Zhong, M.; Jang, M. Dynamic Light Absorption of Biomass-Burning Organic Carbon Photochemically Aged under Natural Sunlight. *Atmos. Chem. Phys.* **2014**, *14* (3).
- (40) Sumlin, B. J.; Pandey, A.; Walker, M. J.; Pattison, R. S.; Williams, B. J.; Chakrabarty, R. K. Atmospheric Photooxidation Diminishes Light Absorption by Primary Brown Carbon Aerosol from Biomass Burning. *Environ. Sci. Technol. Lett.* **2017**, *4* (12).
- (41) Stevens, R.; Dastoor, A. A Review of the Representation of Aerosol Mixing State in Atmospheric Models. *Atmosphere*. 2019.
- (42) Wang, Y.; Hu, M.; Lin, P.; Guo, Q.; Wu, Z.; Li, M.; Zeng, L.; Song, Y.; Zeng, L.;

- Wu, Y.; et al. Molecular Characterization of Nitrogen-Containing Organic Compounds in Humic-like Substances Emitted from Straw Residue Burning. *Environ. Sci. Technol.* **2017**, *51* (11).
- (43) Wang, X.; Heald, C. L.; Liu, J.; Weber, R. J.; Campuzano-Jost, P.; Jimenez, J. L.; Schwarz, J. P.; Perring, A. E. Exploring the Observational Constraints on the Simulation of Brown Carbon. *Atmos. Chem. Phys.* **2018**.
- (44) Brown, H.; Liu, X.; Feng, Y.; Jiang, Y.; Wu, M.; Lu, Z.; Wu, C.; Murphy, S.; Pokhrel, R. Radiative Effect and Climate Impacts of Brown Carbon with the Community Atmosphere Model (CAM5). *Atmos. Chem. Phys.* **2018**.
- (45) *2017 and Later Model Year Light-Duty Vehicle Greenhouse Gas Emissions and Corporate Average Fuel Economy Standards*, Vol. 77.; U.S. Environmental Protection Agency & National Highway Traffic Safety Administration, 2012.
- (46) *2018 EPA Automotive Trends Report*; U.S. Environmental Protection Agency. Data available at www.epa.gov/automotive-trends/explore-automotive-trends-data, Accessed June 04, 2019, 2018.
- (47) *Draft Technical Assessment Report: Midterm Evaluation of Light-Duty Vehicle Greenhouse Gas Emission Standards and Corporate Average Fuel Economy Standards for Model Years 2022-2025 (EPA-420-D-16-900, July 2016)*; U.S. Environmental Protection Agency, 2015.
- (48) Zhao, F.; Lai, M. C.; Harrington, D. L. Automotive Spark-Ignited Direct-Injection Gasoline Engines. *Prog. Energy Combust. Sci.* **1999**, *25* (5), 437–562.
- (49) Smith, O. I. Fundamentals of Soot Formation in Flames with Application to Diesel Engine Particulate Emissions. *Prog. Energy Combust. Sci.* **1981**.

- (50) Barone, T. L.; Storey, J. M. E.; Youngquist, A. D.; Szybist, J. P. An Analysis of Direct-Injection Spark-Ignition (DISI) Soot Morphology. *Atmos. Environ.* **2012**.
- (51) Saliba, G.; Saleh, R.; Zhao, Y.; Presto, A. A.; Lambe, A. T.; Frodin, B.; Sardar, S.; Maldonado, H.; Maddox, C.; May, A. A.; et al. Comparison of Gasoline Direct-Injection (GDI) and Port Fuel Injection (PFI) Vehicle Emissions: Emission Certification Standards, Cold-Start, Secondary Organic Aerosol Formation Potential, and Potential Climate Impacts. *Environ. Sci. Technol.* **2017**, *51* (11), 6542–6552.
- (52) Du, Z.; Hu, M.; Peng, J.; Zhang, W.; Zheng, J.; Gu, F.; Qin, Y.; Yang, Y.; Li, M.; Wu, Y.; et al. Comparison of Primary Aerosol Emission and Secondary Aerosol Formation from Gasoline Direct Injection and Port Fuel Injection Vehicles. *Atmos. Chem. Phys.* **2018**.
- (53) He, L.; Hu, J.; Zhang, S.; Wu, Y.; Zhu, R.; Zu, L.; Bao, X.; Lai, Y.; Su, S. The Impact from the Direct Injection and Multi-Port Fuel Injection Technologies for Gasoline Vehicles on Solid Particle Number and Black Carbon Emissions. *Appl. Energy* **2018**, *226*, 819–826.
- (54) Karavalakis, G.; Short, D.; Vu, D.; Russell, R.; Hajbabaie, M.; Asa-Awuku, A.; Durbin, T. D. Evaluating the Effects of Aromatics Content in Gasoline on Gaseous and Particulate Matter Emissions from SI-PFI and SIDI Vehicles. *Environ. Sci. Technol.* **2015**, *49* (11), 7021–7031.
- (55) Karavalakis, G.; Short, D.; Vu, D.; Villela, M.; Asa-Awuku, A.; Durbin, T. D. Evaluating the Regulated Emissions, Air Toxics, Ultrafine Particles, and Black Carbon from SI-PFI and SI-DI Vehicles Operating on Different Ethanol and Iso-

- Butanol Blends. *Fuel* **2014**, *128*, 410–421.
- (56) Short, D. Z.; Vu, D.; Durbin, T. D.; Karavalakis, G.; Asa-Awuku, A. Components of Particle Emissions from Light-Duty Spark-Ignition Vehicles with Varying Aromatic Content and Octane Rating in Gasoline. *Environ. Sci. Technol.* **2015**, *49* (17), 10682–10691.
- (57) Forestieri, S. D.; Collier, S.; Kuwayama, T.; Zhang, Q.; Kleeman, M. J.; Cappa, C. D. Real-Time Black Carbon Emission Factor Measurements from Light Duty Vehicles. *Environ. Sci. Technol.* **2013**, *47* (22), 13104–13112.
- (58) Chan, T. W.; Meloche, E.; Kubsh, J.; Brezny, R. Black Carbon Emissions in Gasoline Exhaust and a Reduction Alternative with a Gasoline Particulate Filter. *Environ. Sci. Technol.* **2014**, *48* (10), 6027–6034.
- (59) Bahreini, R.; Xue, J.; Johnson, K.; Durbin, T.; Quiros, D.; Hu, S.; Huai, T.; Ayala, A.; Jung, H. Characterizing Emissions and Optical Properties of Particulate Matter from PFI and GDI Light-Duty Gasoline Vehicles. *J. Aerosol Sci.* **2015**, *90*, 144–153.
- (60) Dockery, D. W.; Pope, C. A.; Xu, X.; Spengler, J. D.; Ware, J. H.; Fay, M. E.; Ferris, B. G.; Speizer, F. E. An Association between Air Pollution and Mortality in Fine Particulate Air Pollution and Mortality in Six U.S. Cities. *N. Engl. J. Med.* **1993**, *329* (24), 1753–1759.
- (61) *The Benefits and Costs of the Clean Air Act 1990 to 2010 EPA Report to Congress*; U.S. Environmental Protection Agency, 2010.
- (62) Chung, C. E.; Ramanathan, V.; Decremer, D. Observationally Constrained Estimates of Carbonaceous Aerosol Radiative Forcing. *Proc. Natl. Acad. Sci.*

- 2012**, *109* (29), 11624–11629.
- (63) Zimmerman, N.; Wang, J. M.; Jeong, C. H.; Wallace, J. S.; Evans, G. J. Assessing the Climate Trade-Offs of Gasoline Direct Injection Engines. *Environ. Sci. Technol.* **2016**, *50* (15), 8385–8392.
- (64) Seinfeld, J. H.; Pandis, S. N. *Atmospheric Chemistry and Physics: From Air Pollution to Climate Change, 3rd Edition*; John Wiley & Sons, Inc., Hoboken, New Jersey, 2016.
- (65) Grell, G. A.; Peckham, S. E.; Schmitz, R.; McKeen, S. A.; Frost, G.; Skamarock, W. C.; Eder, B. Fully Coupled “Online” Chemistry within the WRF Model. *Atmos. Environ.* **2005**, *39* (37), 6957–6975.
- (66) Koch, D.; Schulz, M.; Kinne, S.; McNaughton, C.; Spackman, J. R.; Balkanski, Y.; Bauer, S.; Berntsen, T.; Bond, T. C.; Boucher, O.; et al. Evaluation of Black Carbon Estimations in Global Aerosol Models. *Atmos. Chem. Phys.* **2009**, *9* (22), 9001–9026.
- (67) Barnard, J. C.; Fast, J. D.; Paredes-Miranda, G.; Arnott, W. P.; Laskin, A. Technical Note: Evaluation of the WRF-Chem “Aerosol Chemical to Aerosol Optical Properties” Module Using Data from the MILAGRO Campaign. *Atmos. Chem. Phys.* **2010**, *10* (15), 7325–7340.
- (68) Jacobson, M. Z. Investigating Cloud Absorption Effects: Global Absorption Properties of Black Carbon, Tar Balls, and Soil Dust in Clouds and Aerosols. *J. Geophys. Res. Atmos.* **2012**, *117* (6).
- (69) Wang, X.; Heald, C. L.; Ridley, D. A.; Schwarz, J. P.; Spackman, J. R.; Perring, A. E.; Coe, H.; Liu, D.; Clarke, A. D. Exploiting Simultaneous Observational

- Constraints on Mass and Absorption to Estimate the Global Direct Radiative Forcing of Black Carbon and Brown Carbon. *Atmos. Chem. Phys.* **2014**, *14* (20), 10989–11010.
- (70) Kirchstetter, T. W.; Novakov, T.; Hobbs, P. V. Evidence That the Spectral Dependence of Light Absorption by Aerosols Is Affected by Organic Carbon. *J. Geophys. Res. Atmos.* **2004**, *109* (D21).
- (71) Saleh, R.; Hennigan, C. J.; McMeeking, G. R.; Chuang, W. K.; Robinson, E. S.; Coe, H.; Donahue, N. M.; Robinson, A. L. Absorptivity of Brown Carbon in Fresh and Photo-Chemically Aged Biomass-Burning Emissions. *Atmos. Chem. Phys.* **2013**, *13* (15), 7683–7693.
- (72) Chen, Y.; Bond, T. C. Light Absorption by Organic Carbon from Wood Combustion. *Atmos. Chem. Phys. Discuss.* **2009**, *9* (2001), 20471–20513.
- (73) Alexander, D. T. L.; Crozier, P. A.; Anderson, J. R. Brown Carbon Spheres in East Asian Outflow and Their Optical Properties. *Science* (80-.). **2008**, *321* (5890), 833–836.
- (74) Cheng, Z.; Atwi, K.; Onyima, T.; Saleh, R. Investigating the Dependence of Light-Absorption Properties of Combustion Carbonaceous Aerosols on Combustion Conditions. *Aerosol Sci. Technol.* **2019**.
- (75) Saleh, R.; Marks, M.; Heo, J.; Adams, P. J.; Donahue, N. M.; Robinson, A. L. Contribution of Brown Carbon and Lensing to the Direct Radiative Effect of Carbonaceous Aerosols from Biomass and Biofuel Burning Emissions. *J. Geophys. Res.* **2015**, *120* (19), 10285–10296.
- (76) Zhang, A.; Wang, Y.; Zhang, Y.; Weber, R. J.; Song, Y.; Ke, Z.; Zou, Y. Modeling

- the Global Radiative Effect of Brown Carbon: A Potentially Larger Heating Source in the Tropical Free Troposphere than Black Carbon. *Atmos. Chem. Phys.* **2020**.
- (77) Holben, B. N.; Eck, T. F.; Slutsker, I.; Tanré, D.; Buis, J. P.; Setzer, A.; Vermote, E.; Reagan, J. A.; Kaufman, Y. J.; Nakajima, T.; et al. AERONET - A Federated Instrument Network and Data Archive for Aerosol Characterization. *Remote Sens. Environ.* **1998**.
- (78) June, N. A.; Wang, X.; Chen, L. W. A.; Chow, J. C.; Watson, J. G.; Wang, X.; Henderson, B. H.; Zheng, Y.; Mao, J. Spatial and Temporal Variability of Brown Carbon in the United States: Implications for Direct Radiative Effects. *Geophys. Res. Lett.* **2020**.
- (79) Goto, D.; Sato, Y.; Yashiro, H.; Suzuki, K.; Oikawa, E.; Kudo, R.; Nagao, T.; Nakajima, T. Global Aerosol Simulations Using NICAM.16 on a 14-Km Grid Spacing for a Climate Study: Improved and Remaining Issues Relative to a Lower-Resolution Model. *Geosci. Model Dev. Discuss.* **2020**.
- (80) Hu, L.; Keller, C. A.; Long, M. S.; Sherwen, T.; Auer, B.; Da Silva, A.; Nielsen, J. E.; Pawson, S.; Thompson, M. A.; Trayanov, A. L.; et al. Global Simulation of Tropospheric Chemistry at 12.5 Km Resolution: Performance and Evaluation of the GEOS-Chem Chemical Module (V10-1) within the NASA GEOS Earth System Model (GEOS-5 ESM). *Geosci. Model Dev.* **2018**, *11* (11).
- (81) Small, R. J.; Bacmeister, J.; Bailey, D.; Baker, A.; Bishop, S.; Bryan, F.; Caron, J.; Dennis, J.; Gent, P.; Hsu, H. M.; et al. A New Synoptic Scale Resolving Global Climate Simulation Using the Community Earth System Model. *J. Adv. Model.*

- Earth Syst.* **2014**, 6 (4).
- (82) Grell, G. A.; Peckham, S. E.; Schmitz, R.; McKeen, S. A.; Frost, G.; Skamarock, W. C.; Eder, B. Fully Coupled “Online” Chemistry within the WRF Model. *Atmos. Environ.* **2005**, 39 (37), 6957–6975.
- (83) National Centers for Environmental Prediction/National Weather Service/NOAA/U.S. Department of Commerce. NCEP FNL Operational Model Global Tropospheric Analyses, continuing from July 1999. Research Data Archive at the National Center for Atmospheric Research, Computational and Information Systems Laboratory. <https://doi.org/10.5065/D6M043C6> (accessed Jun 5, 2019).
- (84) Stauffer, D. R.; Seaman, N. L.; Binkowski, F. S. Use of Four-Dimensional Data Assimilation in a Limited-Area Mesoscale Model Part II: Effects of Data Assimilation within the Planetary Boundary Layer. *Mon. Weather Rev.* **2002**, 119 (3), 734–754.
- (85) *Technical Support Document (TSD) Preparation of Emissions Inventories for the Version 6.2, 2011 Emissions Modeling Platform*; US Environmental Protection Agency, 2015.
- (86) Larkin, N. K.; Raffuse, S. M.; Huang, S. M.; Pavlovic, N.; Lahm, P.; Rao, V. The Comprehensive Fire Information Reconciled Emissions (CFIRE) Inventory: Wildland Fire Emissions Developed for the 2011 and 2014 U.S. National Emissions Inventory. *J. Air Waste Manag. Assoc.* **2020**.
- (87) Houyoux, M. R.; Vukovich, J. M. Updates to the Sparse Matrix Operator Kernel Emissions (SMOKE) Modeling System and Integration with Models-3. *Proc. Emiss. Invent. Reg. Strateg. Futur.* **1999**.

- (88) National Center for Atmospheric Research (NCAR). EPA_ANTHRO_EMIS tool
<https://www.acom.ucar.edu/wrf-chem/download.shtml> (accessed Jun 6, 2019).
- (89) Wang, J.; Ge, C.; Yang, Z.; Hyer, E. J.; Reid, J. S.; Chew, B. N.; Mahmud, M.; Zhang, Y.; Zhang, M. Mesoscale Modeling of Smoke Transport over the Southeast Asian Maritime Continent: Interplay of Sea Breeze, Trade Wind, Typhoon, and Topography. *Atmos. Res.* **2013**.
- (90) Emmons, L. K.; Walters, S.; Hess, P. G.; Lamarque, J. F.; Pfister, G. G.; Fillmore, D.; Granier, C.; Guenther, A.; Kinnison, D.; Laepple, T.; et al. Description and Evaluation of the Model for Ozone and Related Chemical Tracers, Version 4 (MOZART-4). *Geosci. Model Dev.* **2010**, *3* (1), 43–67.
- (91) Guenther, A.; Karl, T.; Harley, P.; Wiedinmyer, C.; Palmer, P. I.; Geron, C. Estimates of Global Terrestrial Isoprene Emissions Using MEGAN (Model of Emissions of Gases and Aerosols from Nature). *Atmos. Chem. Phys.* **2006**, *6* (11), 3181–3210.
- (92) Zaveri, R. A.; Easter, R. C.; Fast, J. D.; Peters, L. K. Model for Simulating Aerosol Interactions and Chemistry (MOSAIC). *J. Geophys. Res. Atmos.* **2008**, *113* (D13).
- (93) Donahue, N. M.; Robinson, A. L.; Stanier, C. O.; Pandis, S. N. Coupled Partitioning, Dilution, and Chemical Aging of Semivolatile Organics. *Environ. Sci. Technol.* **2006**, *40* (8), 2635–2643.
- (94) Zaveri, R. A.; Easter, R. C.; Peters, L. K. A Computationally Efficient Multicomponent Equilibrium Solver for Aerosols (MESA). *J. Geophys. Res. Atmos.* **2005**, *110* (D24).
- (95) Hodzic, A.; Jimenez, J. L. Modeling Anthropogenically Controlled Secondary

- Organic Aerosols in a Megacity: A Simplified Framework for Global and Climate Models. *Geosci. Model Dev.* **2011**, *4* (4), 901–917.
- (96) Cheng, Z.; Atwi, K.; Hajj, O. El; Ijeli, I.; Fischer, D. Al; Smith, G.; Saleh, R. Discrepancies between Brown Carbon Light-Absorption Properties Retrieved from Online and Offline Measurements. *Aerosol Sci. Technol.* **2021**, *55* (1).
- (97) Dubovik, O.; King, M. D. A Flexible Inversion Algorithm for Retrieval of Aerosol Optical Properties from Sun and Sky Radiance Measurements. *J. Geophys. Res. Atmos.* **2000**.
- (98) Holben, B. N.; Eck, T. F.; Slutsker, I.; Smirnov, A.; Sinyuk, A.; Schafer, J.; Giles, D.; Dubovik, O. Aeronet's Version 2.0 Quality Assurance Criteria. In *Remote Sensing of the Atmosphere and Clouds*; 2006; Vol. 6408.
- (99) Grieshop, A. P.; Donahue, N. M.; Robinson, A. L. Laboratory Investigation of Photochemical Oxidation of Organic Aerosol from Wood Fires 2: Analysis of Aerosol Mass Spectrometer Data. *Atmos. Chem. Phys.* **2009**, *9* (6).
- (100) Hennigan, C. J.; Miracolo, M. A.; Engelhart, G. J.; May, A. A.; Presto, A. A.; Lee, T.; Sullivan, A. P.; McMeeking, G. R.; Coe, H.; Wold, C. E.; et al. Chemical and Physical Transformations of Organic Aerosol from the Photo-Oxidation of Open Biomass Burning Emissions in an Environmental Chamber. *Atmos. Chem. Phys.* **2011**, *11* (15).
- (101) Ortega, A. M.; Day, D. A.; Cubison, M. J.; Brune, W. H.; Bon, D.; De Gouw, J. A.; Jimenez, J. L. Secondary Organic Aerosol Formation and Primary Organic Aerosol Oxidation from Biomass-Burning Smoke in a Flow Reactor during FLAME-3. *Atmos. Chem. Phys.* **2013**, *13* (22).

- (102) Tkacik, D. S.; Robinson, E. S.; Ahern, A.; Saleh, R.; Stockwell, C.; Veres, P.; Simpson, I. J.; Meinardi, S.; Blake, D. R.; Yokelson, R. J.; et al. A Dual-Chamber Method for Quantifying the Effects of Atmospheric Perturbations on Secondary Organic Aerosol Formation from Biomass Burning Emissions. *J. Geophys. Res.* **2017**, *122* (11).
- (103) Decarlo, P. F.; Ulbrich, I. M.; Crouse, J.; De Foy, B.; Dunlea, E. J.; Aiken, A. C.; Knapp, D.; Weinheimer, A. J.; Campos, T.; Wennberg, P. O.; et al. Investigation of the Sources and Processing of Organic Aerosol over the Central Mexican Plateau from Aircraft Measurements during MILAGRO. *Atmos. Chem. Phys.* **2010**, *10* (12).
- (104) Cubison, M. J.; Ortega, A. M.; Hayes, P. L.; Farmer, D. K.; Day, D.; Lechner, M. J.; Brune, W. H.; Apel, E.; Diskin, G. S.; Fisher, J. A.; et al. Effects of Aging on Organic Aerosol from Open Biomass Burning Smoke in Aircraft and Laboratory Studies. *Atmos. Chem. Phys.* **2011**, *11* (23).
- (105) Yokelson, R. J.; Crouse, J. D.; DeCarlo, P. F.; Karl, T.; Urbanski, S.; Atlas, E.; Campos, T.; Shinozuka, Y.; Kapustin, V.; Clarke, A. D.; et al. Emissions from Biomass Burning in the Yucatan. *Atmos. Chem. Phys.* **2009**, *9* (15).
- (106) Tsimpidi, A. P.; Karydis, V. A.; Pandis, S. N.; Lelieveld, J. Global Combustion Sources of Organic Aerosols: Model Comparison with 84 AMS Factor-Analysis Data Sets. *Atmos. Chem. Phys.* **2016**, *16* (14).
- (107) Zimmerman, N.; Wang, J. M.; Jeong, C. H.; Wallace, J. S.; Evans, G. J. Assessing the Climate Trade-Offs of Gasoline Direct Injection Engines. *Environ. Sci. Technol.* **2016**.

- (108) Shindell, D.; Faluvegi, G. Climate Response to Regional Radiative Forcing during the Twentieth Century. *Nat. Geosci.* **2009**, *2*, 294–300.
- (109) Mlawer, E. J.; Taubman, S. J.; Brown, P. D.; Iacono, M. J.; Clough, S. A. Radiative Transfer for Inhomogeneous Atmospheres: RRTM, a Validated Correlated-k Model for the Longwave. *J. Geophys. Res. Atmos.* **1997**, *102* (D14), 16663–16682.
- (110) Bauer, S. E.; Ault, A.; Prather, K. A. Evaluation of Aerosol Mixing State Classes in the GISS ModelE-MATRIX Climate Model Using Single-Particle Mass Spectrometry Measurements. *J. Geophys. Res. Atmos.* **2013**, *118* (17), 9834–9844.
- (111) Feng, Y.; Ramanathan, V.; Kotamarthi, V. R. Brown Carbon: A Significant Atmospheric Absorber of Solar Radiation. *Atmos. Chem. Phys.* **2013**, *13* (17), 8607–8621.
- (112) Jiang, X.; Wiedinmyer, C.; Carlton, A. G. Aerosols from Fires: An Examination of the Effects on Ozone Photochemistry in the Western United States. *Environ. Sci. Technol.* **2012**, *46* (21), 11878–11886.
- (113) Bohren, C. F.; Huffman, D. R. *Absorption and Scattering of Light by Small Particles*; John Wiley & Sons Inc., 1983.
- (114) *Analysis of Particulate Matter Emissions from Light-Duty Gasoline Vehicles in Kansas City*; US Environmental Protection Agency, 2008.
- (115) May, A. A.; Nguyen, N. T.; Presto, A. A.; Gordon, T. D.; Lipsky, E. M.; Karve, M.; Gutierrez, A.; Robertson, W. H.; Zhang, M.; Brandow, C.; et al. Gas- and Particle-Phase Primary Emissions from in-Use, on-Road Gasoline and Diesel Vehicles. *Atmos. Environ.* **2014**, *88*, 247–260.

- (116) US Environmental Protection Agency. Air Quality System Data Mart [internet database] <https://www.epa.gov/airdata> (accessed Oct 1, 2019).
- (117) Tessum, C. W.; Hill, J. D.; Marshall, J. D. Twelve-Month, 12 Km Resolution North American WRF-Chem v3.4 Air Quality Simulation: Performance Evaluation. *Geosci. Model Dev.* **2015**, *8* (4), 957–973.
- (118) Malm, W. C.; Schichtel, B. A.; Pitchford, M. L.; Ashbaugh, L. L.; Eldred, R. A. Spatial and Monthly Trends in Speciated Fine Particle Concentration in the United States. *J. Geophys. Res. Atmos.* **2004**, *109* (D3).
- (119) U.S. Environmental Protection Agency Clean Air Markets Division Clean Air Status and Trends Network (CASTNET) [Meteorological - Hourly] www.epa.gov/castnet (accessed Sep 26, 2019).
- (120) Guenther, A. Seasonal and Spatial Variations in Natural Volatile Organic Compound Emissions. *Ecological Applications*. 1997.
- (121) *Uncertainty Analyses To Support the Second Section 812 Benefit- Cost Analysis of the Clean Air Act*; Industrial Economics Incorporate Office of Air and Radiation US Environmental Protection Agency: Cambridge MA, 2010.
- (122) *Quantitative Health Risk Assessment for Particulate Matter*; U.S. Environmental Protection Agency, 2010.
- (123) Anenberg, S. C.; Talgo, K.; Arunachalam, S.; Dolwick, P.; Jang, C.; West, J. J. Impacts of Global, Regional, and Sectoral Black Carbon Emission Reductions on Surface Air Quality and Human Mortality. *Atmos. Chem. Phys.* **2011**, *11* (14), 7253–7267.
- (124) Krewski, D.; Jerrett, M.; Burnett, R. T.; Ma, R.; Hughes, E.; Shi, Y.; Turner, M.

- C.; Pope, C. A.; Thurston, G.; Calle, E. E.; et al. *Extended Follow-up and Spatial Analysis of the American Cancer Society Study Linking Particulate Air Pollution and Mortality.*; 2009.
- (125) *Guidelines for Preparing Economic Analyses, Updated March 2016*; National Center for Environmental Economics Office of Policy, U. S. Environmental Protection Agency, 2010.
- (126) Karner, A. A.; Eisinger, D. S.; Niemeier, D. A. Near-Roadway Air Quality: Synthesizing the Findings from Real-World Data. *Environ. Sci. Technol.* **2010**, *44* (14), 5334–5344.
- (127) Brugge, D.; Durant, J. L.; Rioux, C. Near-Highway Pollutants in Motor Vehicle Exhaust: A Review of Epidemiologic Evidence of Cardiac and Pulmonary Health Risks. *Environmental Health: A Global Access Science Source*. 2007.
- (128) Guttman, N. B.; Quayle, R. G. A Historical Perspective of U.S. Climate Divisions. *Bulletin of the American Meteorological Society*. 1996.
- (129) Carbon and Other Biogeochemical Cycles. In *Climate Change 2013 the Physical Science Basis: Working Group I Contribution to the Fifth Assessment Report of the Intergovernmental Panel on Climate Change*; 2013.
- (130) Myhre, G.; Shindell, D.; Bréon, F.-M.; Collins, W.; Fuglestedt, J.; Huang, J.; Koch, D.; Lamarque, J.-F.; Lee, D.; Mendoza, B.; et al. Anthropogenic and Natural Radiative Forcing. *Clim. Chang. 2013 Phys. Sci. Basis. Contrib. Work. Gr. I to Fifth Assess. Rep. Intergov. Panel Clim. Chang.* **2013**, 659–740.
- (131) *Fast Facts: U.S. Transportation Sector GHG Emissions*; US Environmental Protection Agency, 2019.

- (132) Shindell, D. T. The Social Cost of Atmospheric Release. *Clim. Change* **2015**, *130* (2), 313–326.
- (133) Wiedinmyer, C.; Akagi, S. K.; Yokelson, R. J.; Emmons, L. K.; Al-Saadi, J. A.; Orlando, J. J.; Soja, A. J. The Fire INventory from NCAR (FINN): A High Resolution Global Model to Estimate the Emissions from Open Burning. *Geosci. Model Dev.* **2011**, *4* (3), 625--641.
- (134) Myhre, G.; Highwood, E. J.; Shine, K. P.; Stordal, F. New Estimates of Radiative Forcing Due to Well Mixed Greenhouse Gases. *Geophys. Res. Lett.* **1998**.
- (135) Hartmann, D. L.; Klein Tank, A. M. G.; Rusticucci, M.; Alexander, L. V.; Brönnimann, S.; Charabi, Y. A. R.; Dentener, F. J.; Dlugokencky, E. J.; Easterling, D. R.; Kaplan, A.; et al. Observations: Atmosphere and Surface. In *Climate Change 2013 the Physical Science Basis: Working Group I Contribution to the Fifth Assessment Report of the Intergovernmental Panel on Climate Change*; 2013.
- (136) International Energy Agency. *CO2 Emissions from Fuel Combustion: Database Documentation*; 2018.
- (137) Trenberth, K. E.; Guillemot, C. J. The Total Mass of the Atmosphere. *J. Geophys. Res.* **1994**.
- (138) Hong, S.-Y.; Noh, Y.; Dudhia, J. A New Vertical Diffusion Package with an Explicit Treatment of Entrainment Processes. *Mon. Weather Rev.* **2006**, *134* (9), 2318–2341.
- (139) Chen, F.; Dudhia, J. Coupling an Advanced Land Surface--Hydrology Model with the Penn State--NCAR MM5 Modeling System. Part I: Model Implementation and Sensitivity. *Mon. Weather Rev.* **2001**, *129* (4), 569–585.

- (140) Paulson, C. A. The Mathematical Representation of Wind Speed and Temperature Profiles in the Unstable Atmospheric Surface Layer. *J. Appl. Meteorol.* **1970**, 9 (6), 857–861.
- (141) Lin, Y.-L.; Farley, R. D.; Orville, H. D. Bulk Parameterization of the Snow Field in a Cloud Model. *J. Clim. Appl. Meteorol.* **1983**, 22 (6), 1065–1092.
- (142) Kain, J. S.; Fritsch, J. M. Convective Parameterization for Mesoscale Models: The Kain-Fritsch Scheme. In *The Representation of Cumulus Convection in Numerical Models*; 1993.

APPENDIX A

SUPPORTING INFORMATION FOR CHAPTER 3

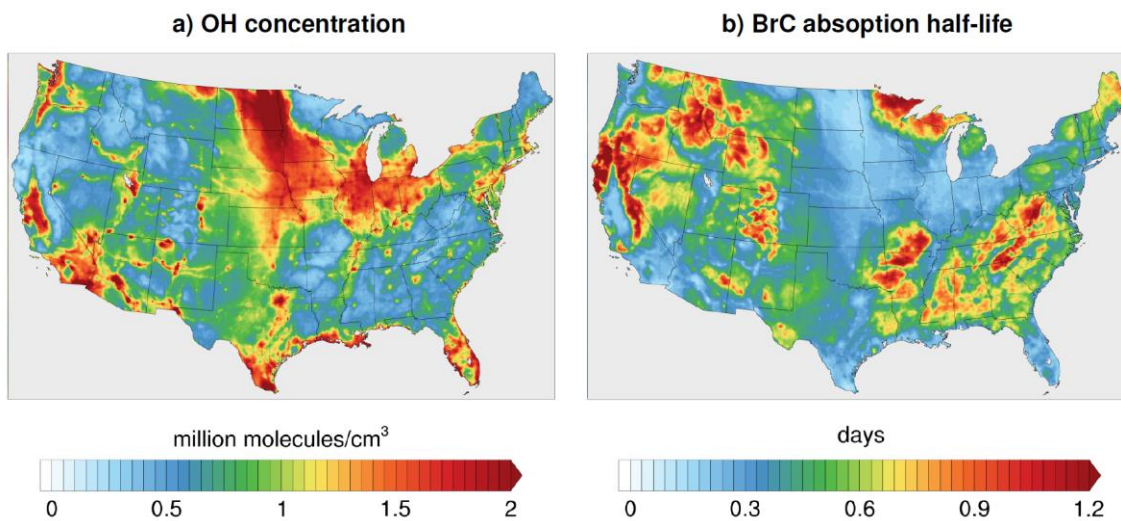


Figure A1. (a) OH concentration averaged over the month of August 2015 and averaged over first 8 vertical layers. (b) BrC absorption half-life averaged over the month of August 2015 and averaged over first 8 vertical layers.

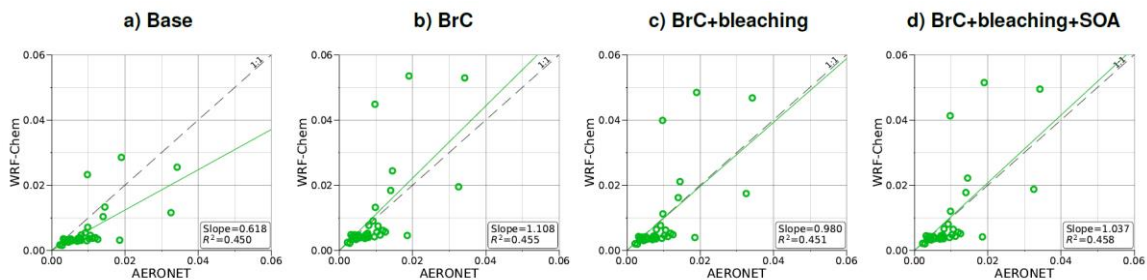


Figure A2. Comparison between monthly average AAOD at 675 nm for August 2015 obtained from AERONET observations and WRF-Chem output with four different model treatments of wildfire carbonaceous aerosol emissions.

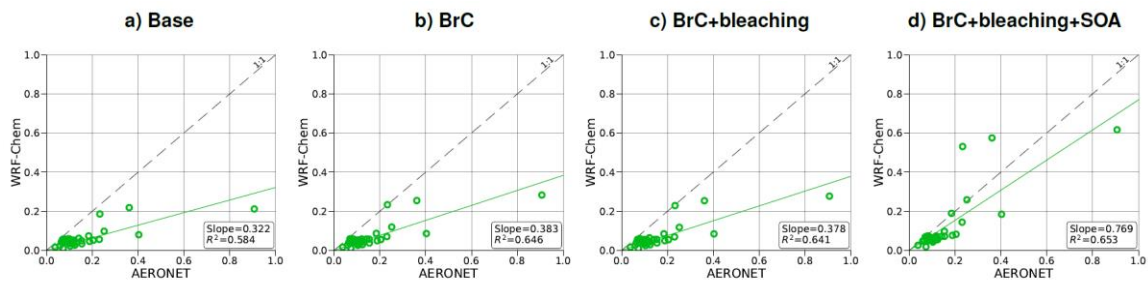


Figure A3. Comparison between monthly average AOD at 675 nm for August 2015 obtained from AERONET observations and WRF-Chem output with four different model treatments of wildfire carbonaceous aerosol emissions.

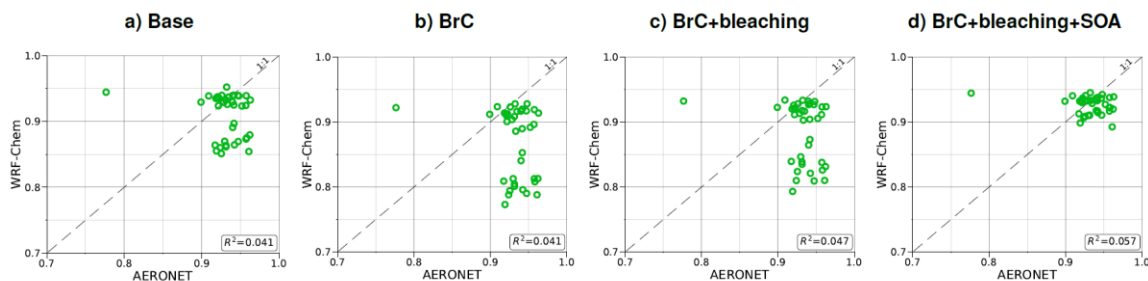


Figure A4. Comparison between monthly average SSA at 675 nm for August 2015 obtained from AERONET observations and WRF-Chem output with four different model treatments of wildfire carbonaceous aerosol emissions.

APPENDIX B

SUPPORTING INFORMATION FOR CHAPTER 4

B.1. Performance Metrics Calculations

Following Boylan and Russell¹ and Tessum et al.¹¹⁷, we assessed the model performance using three performance metrics: normalized mean error (NME), mean fractional error (MFE), and root-mean-square error (RMSE):

$$\text{NME} = \frac{\sum_{i=1}^n |M_i - O_i|}{\sum_{i=1}^n O_i} \quad (\text{B1})$$

$$\text{MFE} = \frac{1}{n} \sum_{i=1}^n \frac{2 \times |M_i - O_i|}{(M_i + O_i)} \times 100 \quad (\text{B2})$$

$$\text{RMSE} = \sqrt{\frac{\sum_{i=1}^n (M_i - O_i)^2}{n}} \quad (\text{B3})$$

Where n is number of stations, M_i denotes time-averaged model concentration at station i , and O_i denotes time-averaged observed concentration at station i .

B.2. Derivation of Attributable Fraction (AF)

Epidemiological data show that premature mortality rates exhibit a log-linear relation with $\text{PM}_{2.5}$ concentrations. The concentration-response factor is defined as the slope of this relation:

$$\beta = \frac{\Delta \ln M}{\Delta C} \quad (\text{B4})$$

Where M represents the premature mortality rate and C represents the PM_{2.5} concentrations.

Equation (B4) can be written for any two M values, M₁ and M₂:

$$\frac{M_2}{M_1} = \text{RR} = \exp(\beta \times \Delta C) \quad (\text{B5})$$

Where RR is the relative risk associated with increasing the PM_{2.5} concentration by ΔC.

Krewski et al.¹²⁴ reported 6% increase in premature mortality (i.e. RR = 1.06) for ΔC = 10 ug/m³. The concentration response factor can therefore be calculated as β = ln(1.06) / 10 = 0.005827.

The attributable fraction, the ratio of premature deaths due to increasing PM_{2.5} concentration by ΔC to total all-cause premature deaths, is defined as:

$$\text{AF} = \frac{(M_2 - M_1)}{M_2} = 1 - \frac{(M_1)}{M_2} = 1 - \exp(-\beta \times \Delta C) \quad (\text{B6})$$

B.3. Calculations Used in Climate-Tradeoff Analysis

We calculated the yearly average radiative effect associated with the reduction in CO₂ emissions due to shifting the global gasoline-vehicle fleet from PFI to GDI using the simplified approximation¹³⁴:

$$\text{RE}_{\text{CO}_2, \text{PFI} \rightarrow \text{GDI}} = 5.35 \times \ln \left(\frac{C_{\text{GDI}}}{C_{\text{PFI}}} \right) \quad (\text{B7})$$

Where C_{PFI} is the yearly average global CO_2 concentration assuming current emission profiles and C_{GDI} is the concentration assuming a complete instantaneous global shift from PFI to GDI.

At year zero, C_{PFI} and C_{GDI} are set to the current level of 400 PPM¹³⁵ ($\sim 0.73 \text{ g/m}^3$). Then for each year, the concentrations are calculated as:

$$C(i) = \frac{[E + C(i-1) \times V]}{V} \quad (B8)$$

Where $C(i)$ and $C(i-1)$ are the yearly average CO_2 concentrations in the current year and previous year, respectively. E is the yearly global CO_2 emission rate, estimated at 33,333 metric tons / year¹³⁶ for the baseline (PFI) scenario. For the GDI scenario, E is estimated based on a 15% reduction in gasoline-vehicle CO_2 emissions⁶³. Since gasoline vehicles contribute approximately 7% of global CO_2 emissions¹³¹, E for the GDI scenario is estimated at 32,983 metric tons / year. $V \approx 3.2 \times 10^{18} \text{ m}^3$ is the volume of the troposphere¹³⁷. We note that while a CO_2 loss rate should be included in equation (B8), the loss rate cancels out in the ratio C_{GDI} / C_{PFI} in equation (B7) and can therefore be ignored.

B.4. Figures

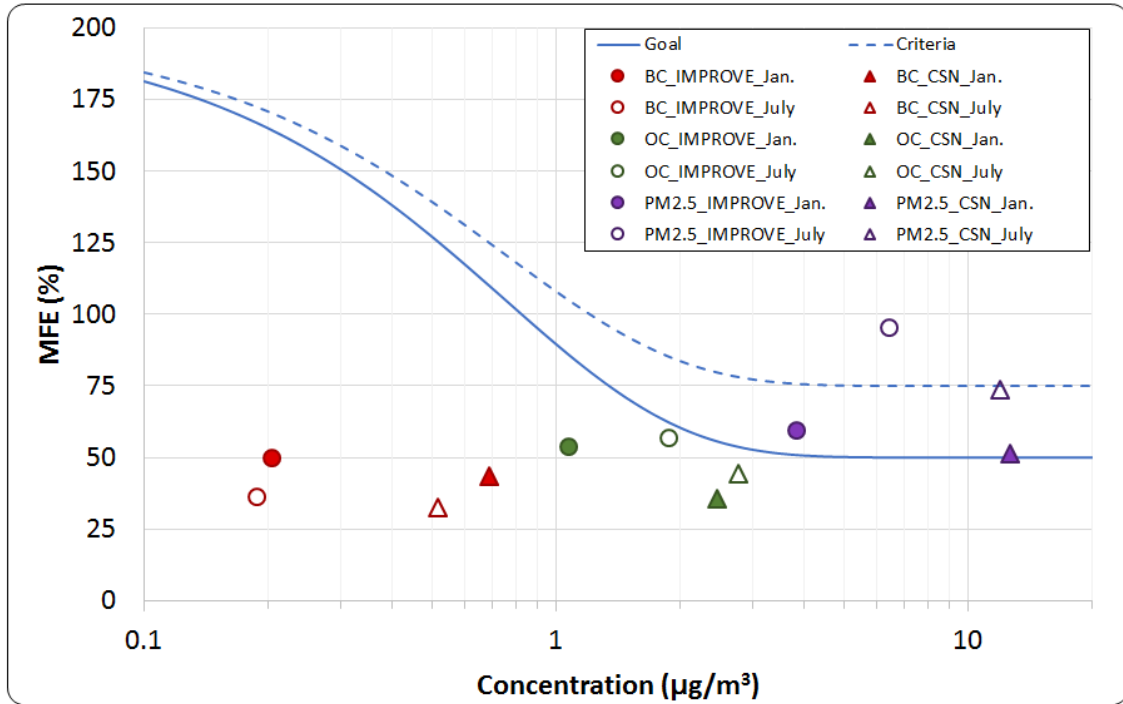


Figure B.1. Comparison of calculated BC (red), OA (green), and PM_{2.5} (purple) MFEs with suggested accuracy levels by Boylan & Russell¹. Circles show calculated MFE based on IMPROVE and triangles show calculated MFE based on CSN network. Filled circles/triangles demonstrate January-averaged, and no-fills are July-averaged.

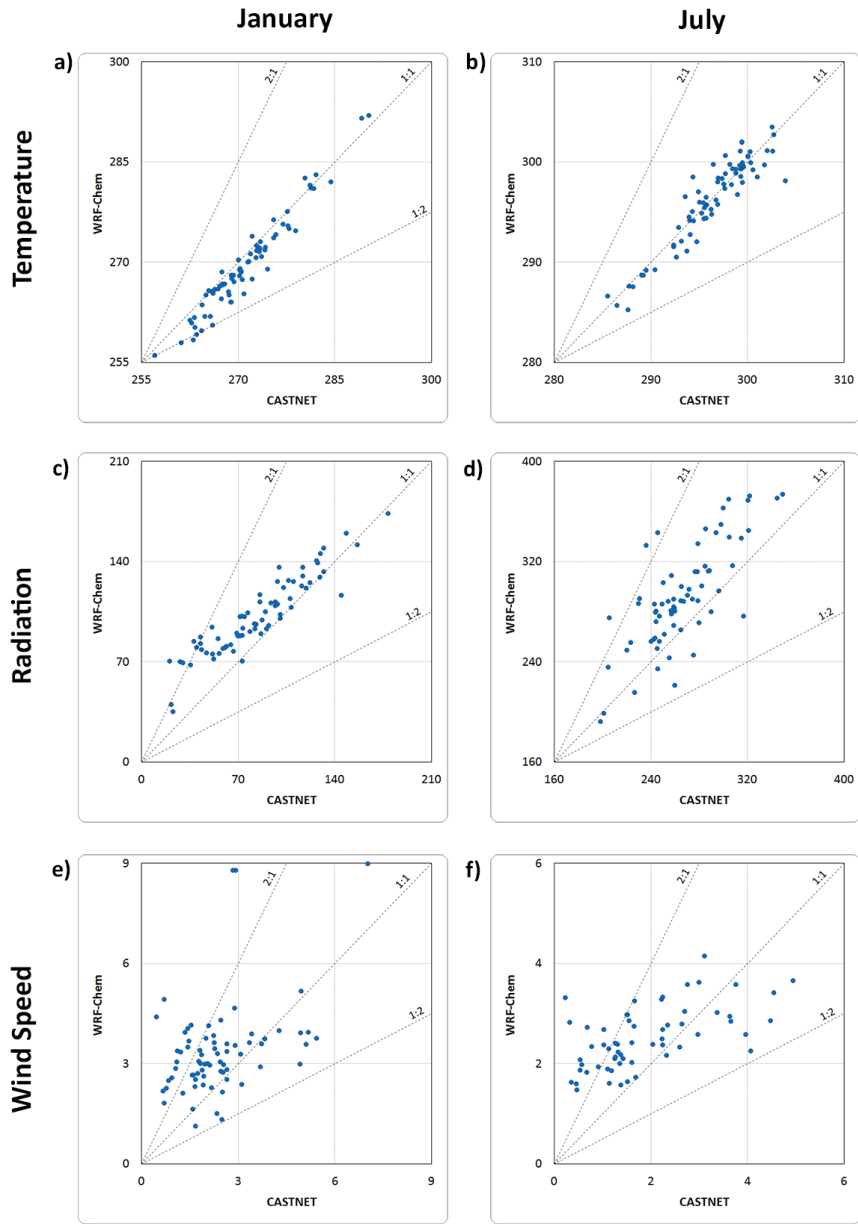


Figure B.2. Comparison between monthly average surface temperature (K), incoming solar radiation flux (W/m^2), and wind speed (m/s) predicted by the model and obtained from CASTNET observational data for 2011. (a) temperature, January. (b) temperature, July. (c) solar radiation, January. (d) solar radiation, July. (e) wind speed, January. (f) wind speed, July.

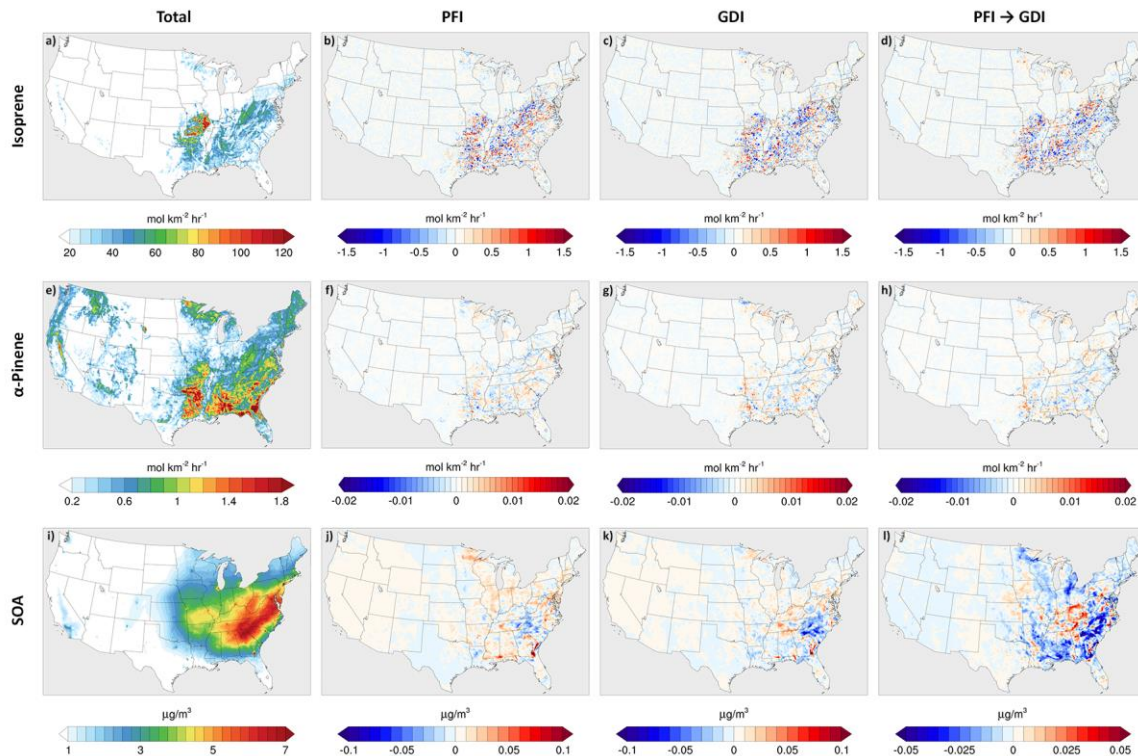


Figure B.3. The Monthly average isoprene emission (top panels), α -Pinene emission (middle panels), and SOA surface concentrations (bottom panels) in July 2011. Panels (a), (e), and (i), obtained from the “PFI” experiments, correspond to the total biogenic emissions and SOA concentrations. Panels (b), (f), and (j), obtained as the difference between the “PFI” and “no-gasoline” experiments, correspond to the contribution of the 2011 gasoline fleet (PFI) to the biogenic emissions and SOA concentrations. Panels (c), (g), and (k), obtained as the difference between the “GDI” and “no-gasoline” experiments, correspond to the contribution of gasoline vehicles to the biogenic emissions and SOA concentrations after shifting to GDI. Panels (d), (h), and (l), obtained as the difference between the “GDI” and “PFI” experiments, correspond to the effect of shifting from PFI to GDI on the biogenic emissions and SOA concentrations.

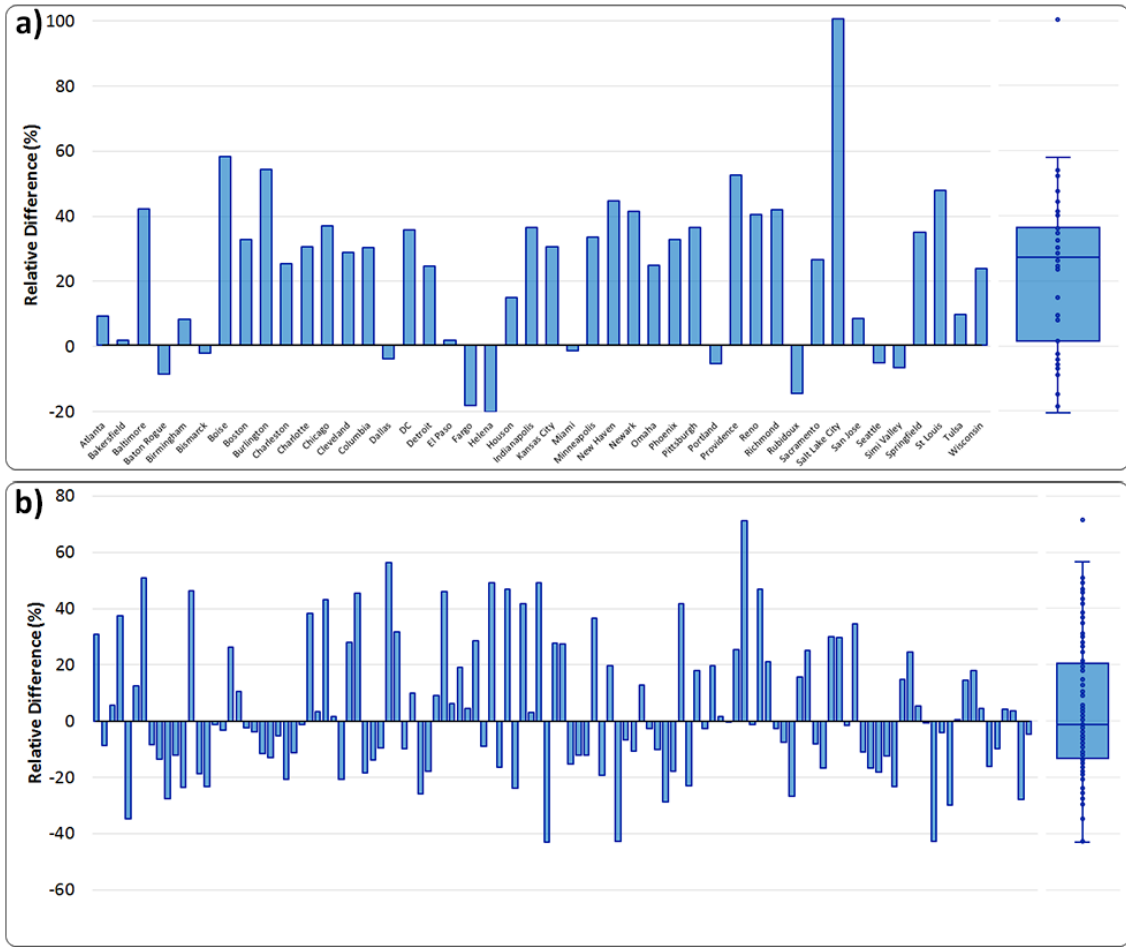


Figure B.4. The relative difference between January/July and annual average PM_{2.5} concentration, based on a) CSN and b) IMPROVE observations.

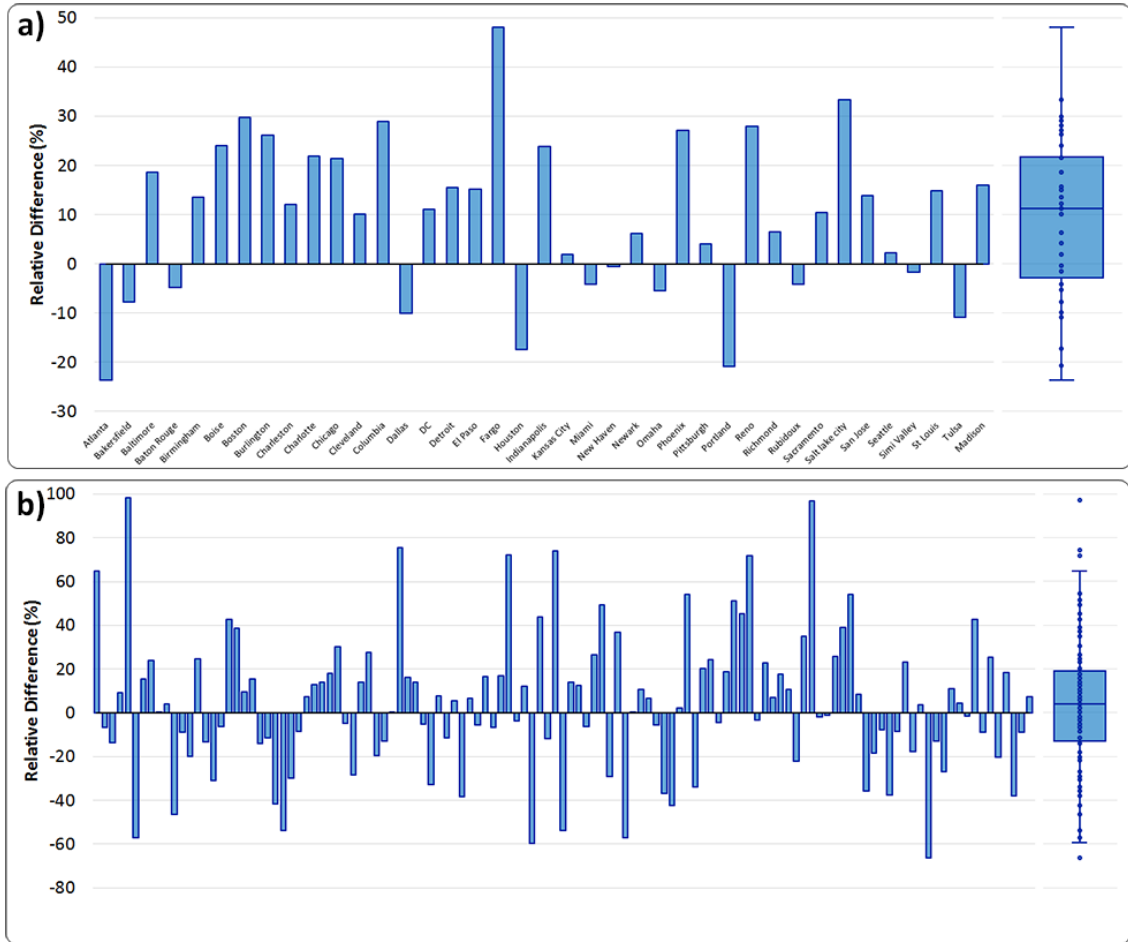


Figure B.5. The relative difference between January/July and annual average carbonaceous (BC + OA) aerosols concentration, based on a) CSN and b) IMPROVE observations.

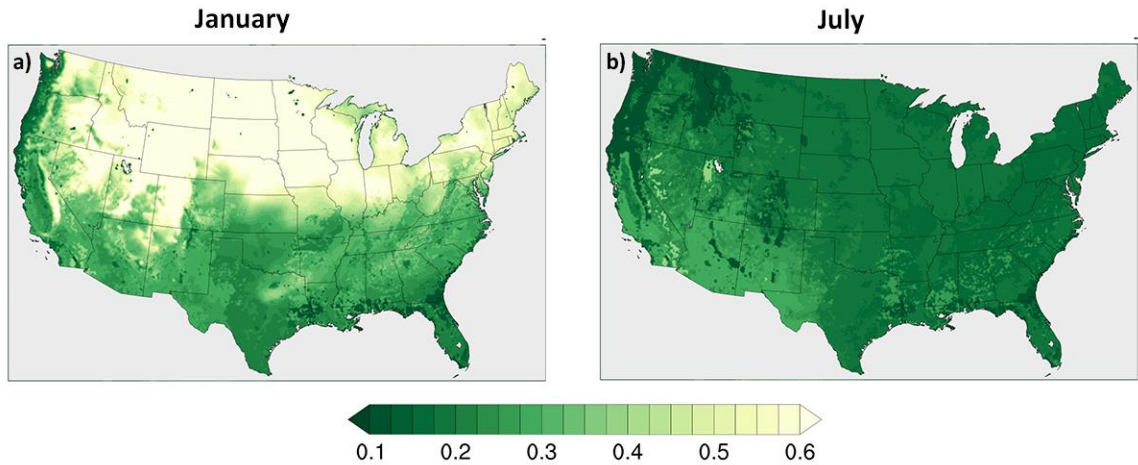


Figure B.6. Monthly average surface albedo in a) January and b) July, 2011.

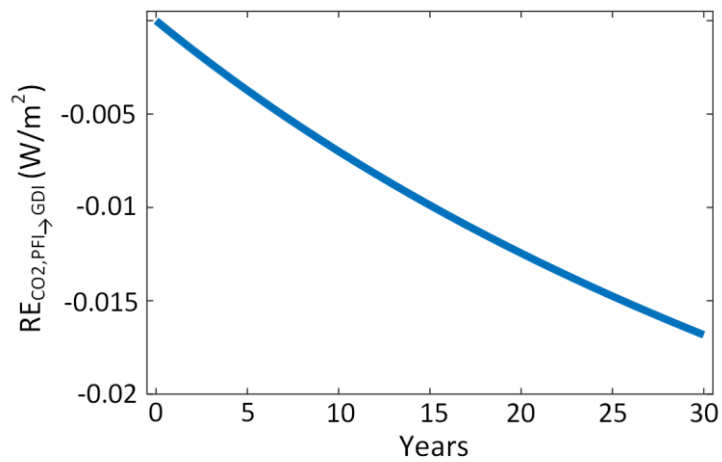


Figure B.7. Yearly average climate benefits quantified as the radiative effect of the reduction in CO₂ emissions associated with a global shift from PFI to GDI.

B.5. Tables

Table B.1. Models and configurations used in WRF-Chem simulations.

Process	Model / Configuration
Planetary boundary layer	Yonsei University method ¹³⁸
Land surface model	NOAH surface model ¹³⁹
Surface layer	National Center for Atmospheric Research (NCAR) / Penn State Mesoscale Model (MM5) ¹⁴⁰
Microphysics	Lin ¹⁴¹
Cumulus parameterization	Kain-Fritsh ¹⁴²
Meteorological boundary/initial conditions and data assimilation	National Center for Environmental Prediction (NCEP) final reanalysis data ⁸³
Biomass-burning emissions	Fire Inventory from NCAR (FINN) ¹³³
Bio-emissions	Model of Emissions of Gases and Aerosols from Nature (MEGAN) ⁹¹
Gas-phase chemistry	Model for Ozone and Related Chemical Tracers (MOZART) ⁹⁰
Aerosol process	Model for Simulating Aerosol Interactions and Chemistry (MOSAIC) ⁹²

Table B.2. Calculated performance metrics (NME, MFE, and RMSE) for monthly-averaged model results.

Month	Parameter	Observation	NME (%)	MFE (%)	RMSE
Jan.	BC	IMPROVE	43.4	32.9	0.16
		CSN	42.8	28.5	0.40
	OA	IMPROVE	68.9	39.5	1.41
		CSN	47.7	30.0	1.74
	PM_{2.5}	IMPROVE	48.8	44.3	2.96
		CSN	47.4	36.2	7.83
	Temperature	CASTNET	0.8	0.5	2.58
	Solar radiation	CASTNET	21.7	18.0	22.06
	Wind speed	CASTNET	54.5	36.4	1.73
	July	BC	IMPROVE	34.1	22.7
CSN			30.3	20.8	0.25
OA		IMPROVE	47.6	28.3	1.36
		CSN	38.1	24.3	1.18
PM_{2.5}		IMPROVE	60.4	63.0	4.43
		CSN	51.2	43.0	6.79
Temperature		CASTNET	0.4	0.3	2.58
Solar radiation		CASTNET	11.3	7.3	36.18
Wind speed	CASTNET	49.7	39.0	1.12	